PAPER I

ANALYSIS OF THE VSP-CDP MAPPING ALGORITHM

Spyros K. Lazaratos

ABSTRACT

It has been recently demonstrated (Lazaratos et al., 1991 and 1992) that the VSP-CDP mapping is an appropriate and robust algorithm for crosswell reflection imaging. Although the mapping is widely used with offset-VSP data, fundamental issues associated with its performance have not, to my knowledge, been published in the open litterature. Such issues include the sensitivity of the algorithm to dip and velocity errors, algorithm-induced distortions of the image, as well as lateral resolution considerations (size of the Fresnel zone for the crosswell recording geometry). These issues are addressed in this paper. The results presented here are important for the better understanding of the algorithm's results and the interpretation of mapped crosswell data.

INTRODUCTION

A variety of approaches for crosswell full-waveform imaging applications have been proposed in recent years. Most of the more recent theoretical developments are different types of wave-theoretic imaging algorithms, ranging from migration (Hu et al., 1988), to acoustic (Devaney, 1984; Harris, 1987; Miller at al., 1987; Wu and Toksöz, 1987, Lo et al., 1988; Woodward, 1989; Pratt and Worthington, 1990a) and elastic (Beydoun et al., 1989; Beydoun and Mendes, 1989; Pratt and Worthington, 1990b) diffraction tomography and non-linear inversion (Luo and Schuster, 1990). Although these algorithms represent significant theoretical developments, their wide-aperture spatial impulse response makes them sensitive to problems often encountered in real crosswell data applications, like noise, imperfect amplitude balancing, inaccurate velocity backgrounds and limited aperture. Noise gets smeared by the long impulse response of the imaging operator and gives rise to migration smiles that make the interpretation of individual gathers confusing. Any amplitude variation that is not explained by the wave-propagation model used by the imaging algorithm will produce similar effects. Non-repeatable coupling of sources and receivers to the formation and unknown radiation patterns are two sources of amplitude variation that are difficult to take into account. Corrections for geometric spreading and transmission losses will only be appropriate if the velocity model used for imaging is very close to the true model. Inaccurate velocity models will, not only, misposition events but also generate imperfect amplitude corrections and additional artifacts. Edge effects, due to limited aperture, are also known to adversely affect migration-type algorithms. The studies mentioned above have improved our theoretical understanding of the imaging procedure, but the robust application of wave-theoretic imaging algorithms to real crosswell data requires additional research.

On the other hand, in the majority of the, relatively few, real-data studies, a ray-theoretic imaging algorithm, the VSP-CDP (Vertical Seismic Profile to Common Depth Point) mapping was used (Baker and Harris, 1984; Iverson, 1988, Abdalla et al., 1991). This algorithm was first introduced by Wyatt and Wyatt (1981) and it has since been a very popular method of imaging offset-VSP data.

Unlike the wave-theoretic algorithms, whose long impulse responses change significantly the appearance of the data, the VSP-CDP mapping is a point-to-point transformation (every data sample maps to a single point in the image) more similar to the normal moveout correction (NMO) than to migration. It is robust because it essentially amounts to a different way of looking at the data, without operating on them as drastically as the wave-theoretic algorithms do. It is exactly invertible, independent of aperture limitations. Because of its robustness, the VSP-CDP mapping was the imaging algorithm used in all the real-data studies in this thesis.

Although ray-theoretic imaging is robust, this advantage comes at a price. Mapping algorithms need to be given the dip to correctly map the data. They also stretch the data during mapping, thus limiting resolution. Their lateral resolution is fundamentally limited by their inability to collapse the Fresnel zone. This limitation is particularly significant for wide-angle reflections, because the size of the Fresnel zone increases with the angle of incidence.

In this paper an analysis of issues associated with the reflection-mapping algorithm is presented. These issues are the performance of mapping in the presence of in-plane and out-of-plane dips, its sensitivity to inaccurate velocities, the stretching distortions introduced to the data and the limits of lateral resolution as predicted by the construction of Fresnel zones. The results presented here are important for the better understanding of the algorithm's results and the interpretation of mapped crosswell data.

ALGORITHM DESCRIPTION

Although the VSP-CDP mapping is a well-known algorithm for offset-VSP data processing, it is briefly described in this section for the benefit of readers that might be unfamiliar with the technique. Some implementation details are also discussed.

The basic idea behind the VSP-CDP mapping is explained in Figure 1. Given a source-receiver pair, a trajectory can be defined that links all the possible reflection points for reflections recorded in this trace. For a horizontal reflector at a depth z_A, the corresponding reflection point is A, for a horizontal reflector at a depth z_B, the corresponding reflection point is B, for a horizontal reflector at a depth z_C, the corresponding reflection point is C and so on. The mapping trajectory is defined by linking the possible reflection points for all depths. Once the trajectory is defined, every sample of this trace is mapped on the reflection point for which the total reflection traveltime is equal to the time this sample is recorded. This procedure is repeated for all traces in the gather.

For a constant velocity, the mapping trajectories and corresponding traveltimes can be calculated analytically. For more general velocity backgrounds, they can be calculated by ray tracing. A 1-D velocity model is shown in Figure 2a. Mapping

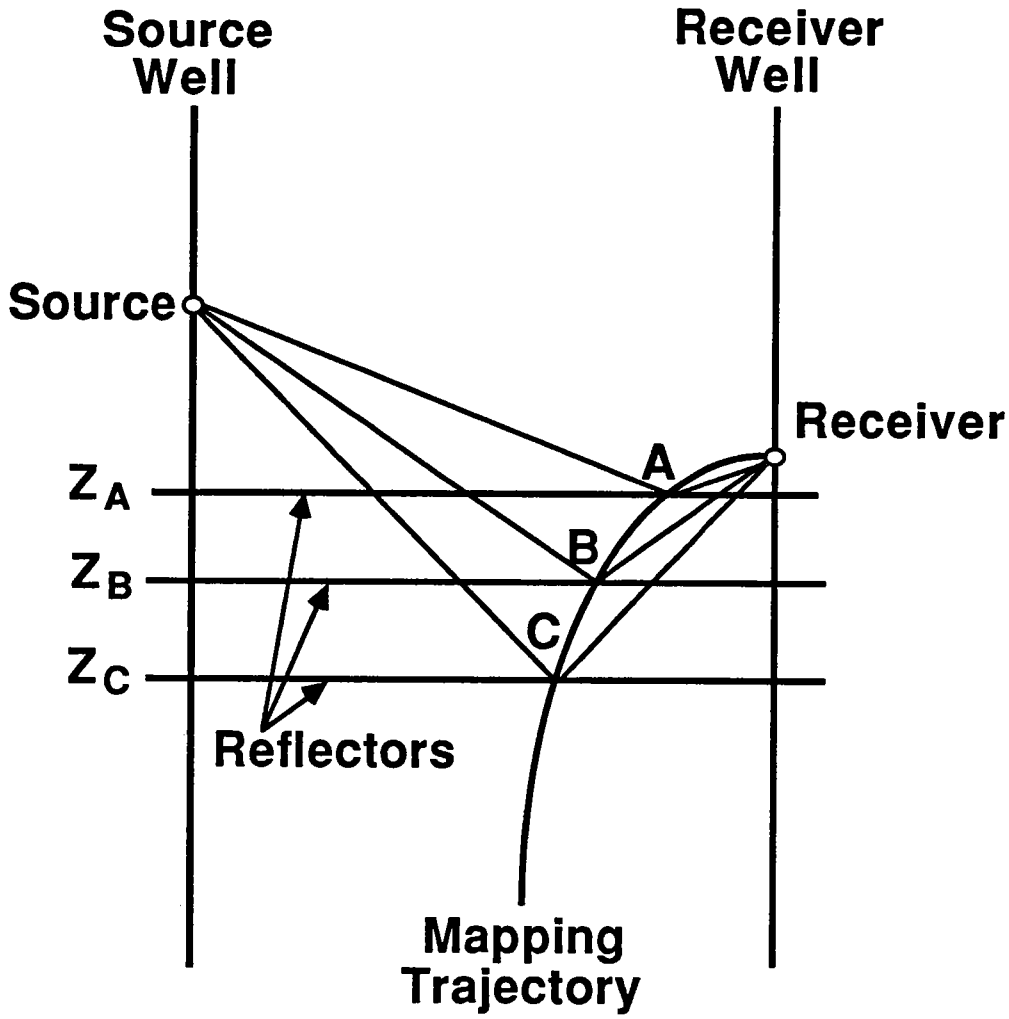

Figure 1: Construction of mapping trajectories.

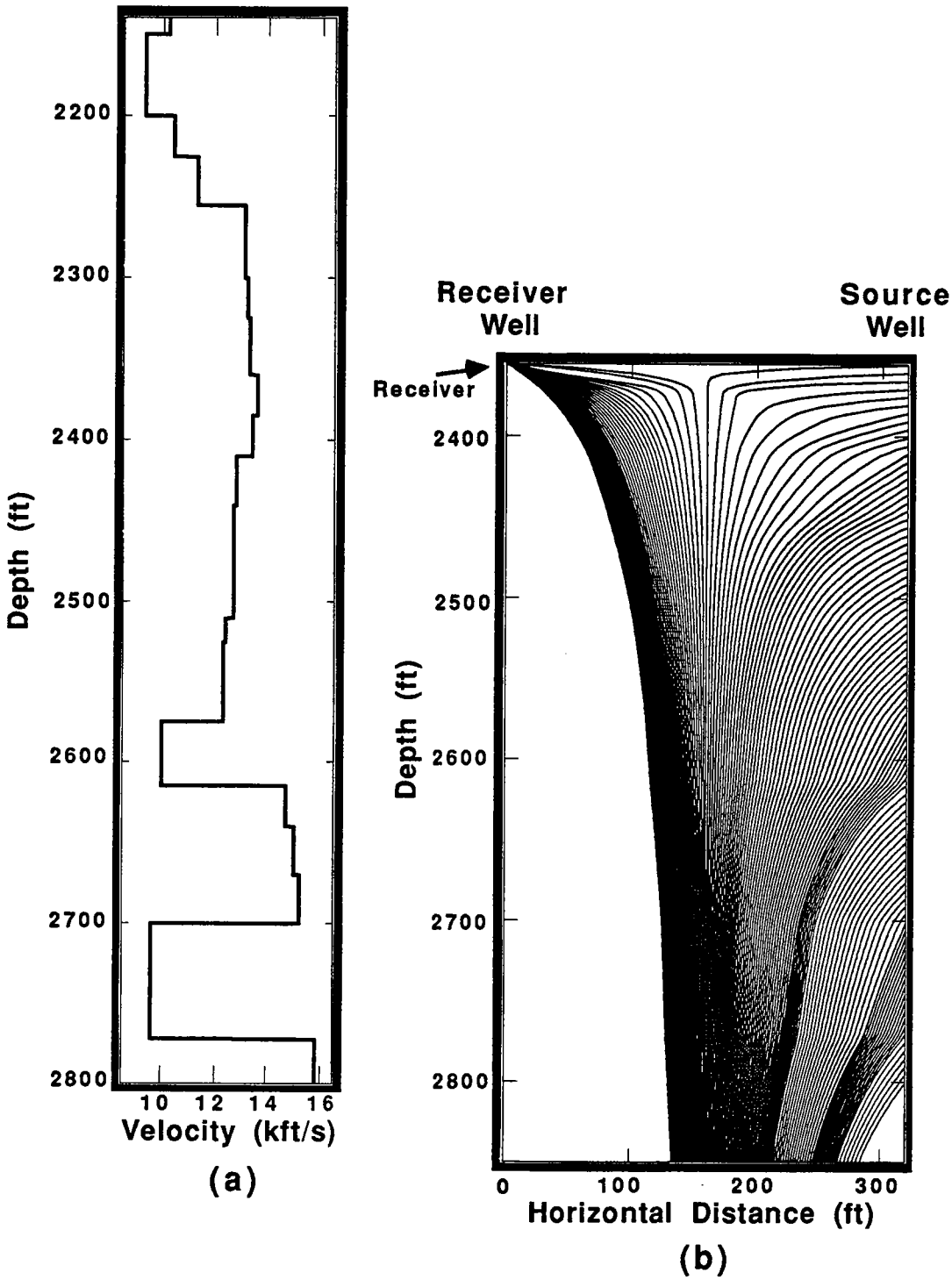

Figure 2: (a) A 1-D velocity model. (b) Mapping trajectories for a common-receiver gather, calculated by ray-tracing through the model in (a).

trajectories, calculated by ray tracing through this model, are shown in Figure 2b. These are trajectories for a common-receiver gather. Every trajectory corresponds to a source Trajectories that start from the source well (on the right-hand part of the plot) correspond to sources located at depths larger than the receiver depth. The group of trajectories that start from the receiver location (on the left-hand part of the plot) corresponds to sources located at depths smaller than the receiver depth.

Although the algorithm was conceptually described as the operation of spreading traces along the reflection point trajectories, the actual implementation that was used in this thesis is different. It is based on the generation of maps, attributing to each point in the image the following quantities:

- Depth of the receiver (source for a common-receiver gather) at which a specular reflection for a horizontal reflector passing through this point will be recorded.
- Reflection traveltime.
- Reflection moveout. This is the dip of the reflection event in the data.

Figure 3 shows contour plots of these maps, calculated for the velocity model of Figure 2. Since the mapping trajectories connect reflection points corresponding to a constant source depth (for a common-receiver gather), they are, by definition, identical to the contours of the source-depth map (compare Figures 2 and 3).

Once these maps are calculated, the imaging is performed by assigning to each point in the image a data value corresponding to the source (for a common-receiver gather) depth and time given from the maps. Since the data are discrete, an interpolation step is necessary. The moveout map, defining the dip of the reflection events, is used at this stage: interpolating along the dip of the reflection events allows the use of simple interpolators that work well even for sparsely sampled data. As a practical consideration, in order to preserve the wavelet character, some smoothing of the maps is performed before imaging.

MAPPING VS. MIGRATION

The VSP-CDP mapping is not a migration algorithm: migration handles correctly all dips while the mapping is accurate only for horizontal reflectors. This can be remedied if the local dip is known. Then we can similarly derive a mapping algorithm that correctly images events with the desirable dip. Still, though, mapping algorithms can handle only a single dip at a time, while migration can handle a range of dips. Imaging ranges of dips correctly is necessary to collapse diffractions and remove the effects of interference from scatterers within the first Fresnel zone. So, even when the reflectors have the dip that the mapping algorithm assumes, migration is still needed to improve the lateral resolution by collapsing the Fresnel zone. Since the mapping is a point-to-point transformation, not altering the original data values, migration could be applied after mapping.

The mapping can be considered the limit of migration as the aperture of the migration operator goes to zero. This is illustrated in Figures 4 and 5. In Figure 4 I show contours of traveltime maps calculated for the 1-D velocity model of Figure

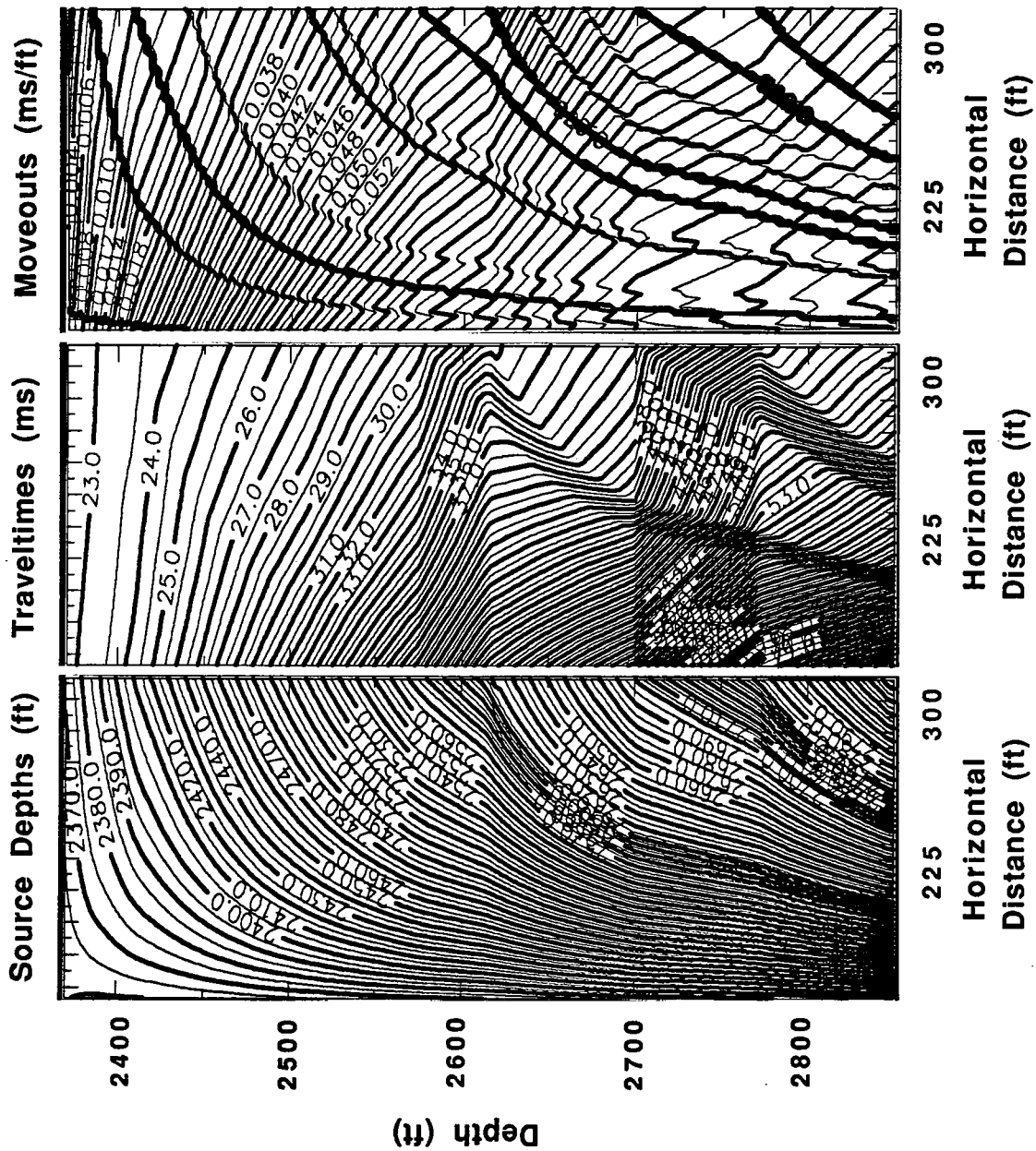

Figure 3: Maps of quantities used for imaging.

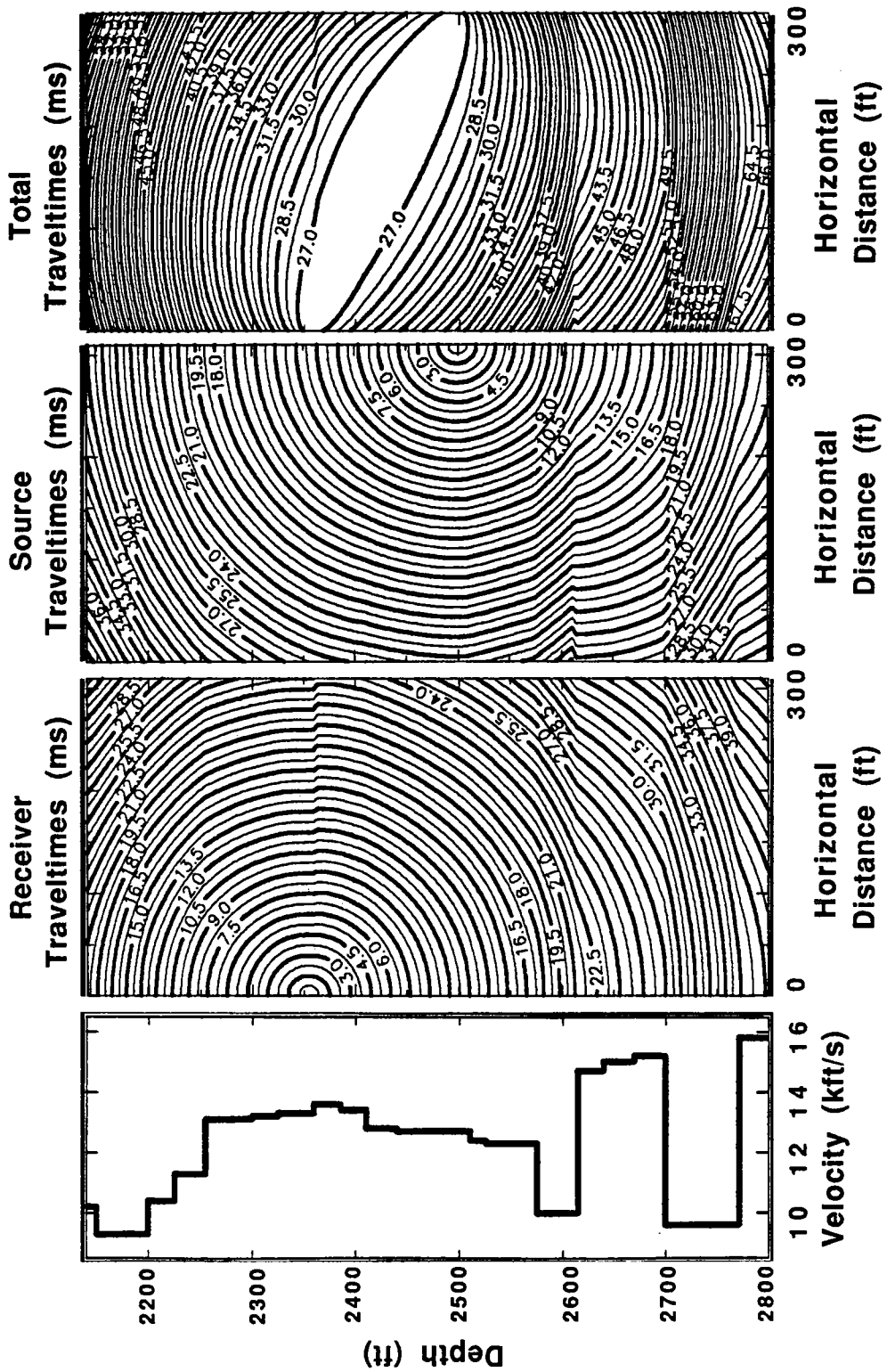

Figure 4: Traveltime maps used to calculate the migration impulse response. Maps correspond to a receiver depth of 2355 ft, a source depth of 2500 ft and the 1-D velocity model shown here.

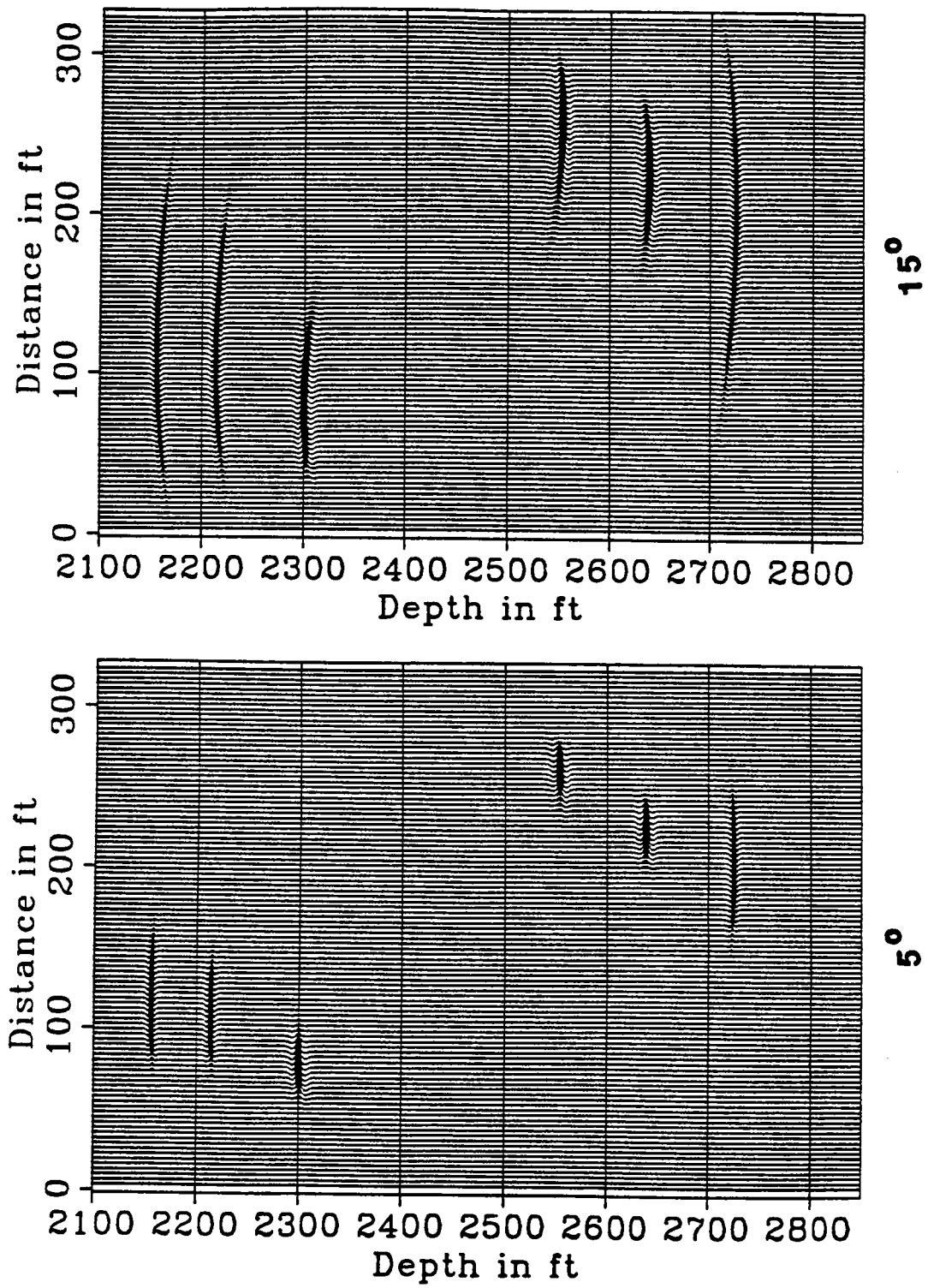

Figure 5: Limited aperture migration operators.

2. The first two parts of Figure 4 are the traveltimes from a receiver/source to all the points in the medium we want to image. The third is the sum of the first two and its contours are often called isochrone trajectories. For a constant-velocity medium, these trajectories are elliptical. In the example of Figure 4, the ellipses are distorted because the velocity model is heterogeneous. Migration essentially amounts to spreading each data point on the appropriate distorted ellipse. We could spread it on the whole ellipse or on a part of it only. Using only part of the ellipse means restricting the imaging to a range of dips. In Figure 5 we give two examples of possible migration operators. This figure shows how migration images a single trace containing three spikes. The trace corresponds to the source-receiver pair for which the migration ellipses have been drawn in Figure 4. Full-aperture migration would spread the spikes on the whole ellipses. The operators illustrated here spread them on parts of ellipses. The operator shown on the left plot can correctly image a 5^0 range of dips around zero dip. The operator on the right is valid for a 15^0 range of dips. As we make the aperture (dip range) narrower and narrower, the smiles shown on these plots tend to collapse and eventually become points on a trajectory like the ones in Figure 2.

Although migration has a number of theoretical advantages over the mapping (correct handling of dipping reflectors without the need to know the dip a priori, collapse of diffractions, shrinking of the Fresnel zone), its performance significantly degrades with noisy data. Notice in Figure 5 how wide the migration operator becomes, when we try to image rather moderate dips of 15^0. A single spike in the data can spread over three quarters of the image. Crosswell data are contaminated by strong noise even after wavefield separation. Spreading noise along the migration impulse response makes event identification ambiguous. Migration is also sensitive to limited recording aperture, gaps in the coverage and imperfect amplitude recovery.

On the other hand, the mapping is a point-to-point transformation: each data sample is mapped to a single point in the image. So, the appearance of the data is better preserved. The mis-interpretation of smeared noise events for signal is less likely. Distortions are still introduced though, since the mapping is nothing more than a global stretch of the data. These distortions are similar to the NMO stretch and are examined in a following section.

IMAGING DIPPING REFLECTORS

As explained in the previous sections, the mapping algorithm needs to be given the dip to correctly image the data. When the assumed dip differs from the true dip, reflection events are mapped to incorrect spatial locations. In this section I examine the order of magnitude and nature of the errors that are produced when dipping reflectors are mapped under the assumption that they are horizontal.

The basic geometry that we are going to consider is shown in Figure 6. The analysis here is restricted to the simple case of a single dipping interface in a constant velocity medium. The two wells are assumed to be vertical. The dipping reflector is defined by the dip angle θ and the azimuth angle α. The latter is the angle a dip line on the reflector forms with the plane of the two wells.

The reason dipping reflectors cause mapping errors is outlined in Figure 7. For clarity I show the case when the reflector dip direction lies in the plane of the wells. Suppose we record a reflection from point A on the dipping reflector. Since our mapping algorithm assumes reflectors are horizontal, the data sample that should be mapped to point A will instead be mapped to point B. Point B is a reflection point on a horizontal reflector such that the total traveltime for the reflection from B equals the total traveltime for the reflection from A. Both A and B lie on an ellipse whose foci are the source and receiver positions. This is the familiar migration ellipse. The total traveltime for a reflection (or scattering) produced from any point on the ellipse is constant for this source/receiver pair. The dipping reflector is tangent to the ellipse at point A and the horizontal reflector is tangent to the ellipse at point B.

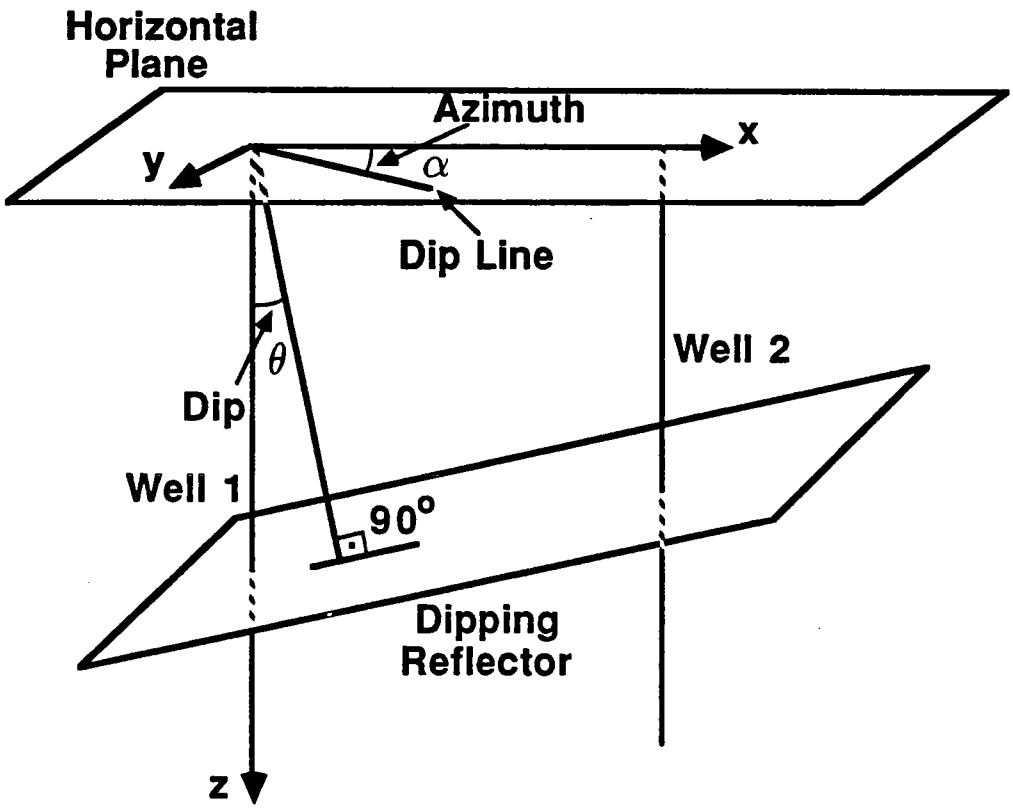

Figure 6: Out-of-plane dipping reflector.

Given the horizontal coordinate x_{hor} of point B and the apparent angle of incidence ϕ for the horizontal reflector, the ellipse can be defined. Then we can define point A as the point of the ellipse where the tangent has a slope θ equal to the dip of the dipping reflector.

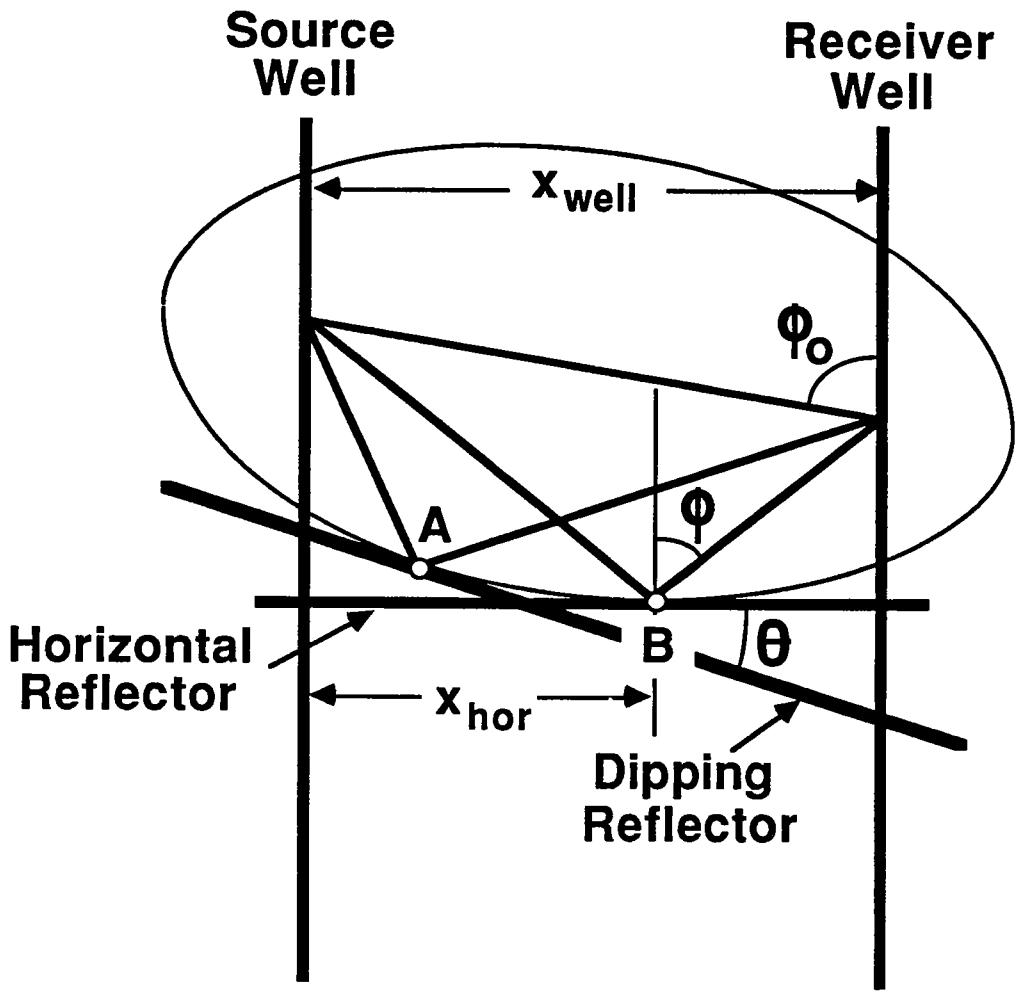

Figure 7: Reflection point mispositioning due to dip.

For the case of out-of-plane dip, the ellipse has to be replaced by an ellipsoid. In this case point A will be the point where the dipping reflector is tangent to the ellipsoid.

The calculations that define the coordinates of the real reflection point A given the horizontal coordinate x_{hor} of point B and the apparent angle of incidence ϕ are explained in Appendix A. The final result is given below.

$$\frac{x_{hor} - x_{dip}}{x_{well}} = \frac{\tan\phi}{2\tan\phi_0} - \frac{a_0^2\lambda_1 \sin\phi_0 - b_0^2\lambda_3\cos\phi_0}{\sqrt{a_0^2\lambda_1^2 + b_0^2(\lambda_2^2+\lambda_3^2)}} \tag{1}$$

$$\frac{y_{hor} - y_{dip}}{x_{well}} = \frac{b_0^2\lambda_2}{\sqrt{a_0^2\lambda_1^2 + b_0^2(\lambda_2^2+\lambda_3^2)}} \tag{2}$$

$$\frac{z_{hor} - z_{dip}}{x_{well}} = \frac{1}{2\tan\phi} - \frac{a_0^2\lambda_1\cos\phi_0 + b_0^2\lambda_3\sin\phi_0}{\sqrt{a_0^2\lambda_1^2 + b_0^2(\lambda_2^2+\lambda_3^2)}} \tag{3}$$

where

$$a_0 = \frac{1}{2\sin\phi} \tag{4}$$

$$b_0 = \frac{\sqrt{\sin^2\phi_0 - \sin^2\phi}}{2\sin\phi\sin\phi_0} \tag{5}$$

$$\lambda_1 = \cos\phi_0\cos\theta - sin\phi_0\sin\theta\cos\alpha \tag{6}$$

$$\lambda_2 = \sin\theta\sin\alpha \tag{7}$$

$$\lambda_3 = \sin\phi_0\cos\theta + \cos\phi_0\sin\theta\cos\alpha \tag{8}$$

and ϕ_0 is the angle formed by the source-receiver raypath and the vertical (see Figure 7) This angle can be calculated from the equation

$$\tan\phi_0 = \frac{\tan\phi}{2(\frac{x_{hor}}{x_{well}}) - 1} \tag{9}$$

In the above equations $(x_{dip}, y_{dip}, z_{dip})$ are the coordinates of the true reflection point (the reflection point on the dipping reflector, point A in Figure 7) and $(x_{hor}, y_{hor}, z_{hor})$ are the coordinates of the reflection point under the assumption that the reflectors are horizontal (point B in Figure 7). The interwell distance is x_{well}. So, equations (1) to (9) describe the lateral, out-of-plane and vertical mispositioning of the reflection point due to the horizontal-reflector assumption as a fraction of the distance between wells. They represent the straight-ray corrections that would need to be applied to data mapped with the horizontal-reflector algorithm to correct for the effect of dip.

From the above equations we can see that the mispositioning due to dip is proportional to the interwell distance and does not depend on the velocity of the medium, when raypaths are straight. For a given dip and azimuth it depends on the apparent angle of incidence ϕ and on the lateral location of the mispositioned reflection point expressed as a fraction of the interwell distance (x_{hor}/x_{well} in equation (9)).

We are now going to use equations (1) to (9) to get a qualitative understanding of dip-induced mispositioning of the reflection point through a sequence of numerical examples. Our conclusions will be exact only for the case of straight raypaths but we can expect them to be qualitatively correct when ray bending is not very significant.

We start with the case of in-plane dips. The basic geometry is the one in Figure 7. Reflectors dip from left to right and the horizontal coordinate is the distance from the left well. Figure 8 shows the vertical and lateral mispositionings of the reflection point as fractions of the interwell distance ($(z_{hor} - z_{dip})/x_{well}$ and $(x_{hor} - x_{dip})/x_{well}$). These mispositionings are plotted as functions of the normalized horizontal coordinate of the mispositioned reflection point (x_{hor}/x_{well}). The results in Figure 8 are for an apparent angle of incidence (angle of incidence under the horizontal reflector assumption, ϕ in equations (1) to (9)) of 45^0 and for a sequence of in-plane dips ranging from 5^0 to 25^0.

Figure 8 shows that both vertical and lateral mispositionings are zero at the two wells (when x_{hor}/x_{well} equals 0 or 1). This is generally valid for in-plane or out-of-plane dips and whether the raypaths are straight or not. For reflection points at the wells, the traveltime for the reflection is the same as the traveltime for the direct arrival. This implies that the data samples that will be mapped to these reflection points will be the intersections of the reflection events with the direct arrival independent of dip or velocity assumptions. This is shown schematically in Figure 9. Stated differently, this observation means that, if the velocity model used for imaging fits the direct arrival traveltimes, the reflection images should tie the logs at the two wells independent of the assumed and actual dips of the reflectors.

Figure 8 shows that both lateral and vertical mispositionings get larger with increasing dips and also that lateral mispositioning is much more significant than vertical mispositioning. For a dip of 10^0, the maximum vertical mispositioning is of the order of 2 percent of the distance between wells, while the maximum horizontal mispositioning is of the order of 20 percent of the distance between wells. This is true for all angles of incidence, as is demonstrated in Figure 10, which shows the lateral and vertical mispositionings for a constant dip of 10^0 and incidence angles ranging from 20^0 to 80^0.

Another way to look at these results is by showing the images of dipping reflectors mapped with a horizontal-reflector algorithm. These can also be calculated from equations (1) to (9) as follows: given the coordinates (x_{dip}, z_{dip}) of a reflection point on a dipping reflector, equations (1) to (9) can be inverted numerically for x_{hor} and z_{hor}. Repeating this for all points along the dipping reflector, we can calculate the image of this reflector under the horizontal-reflector assumption.

The result of this procedure for five dipping reflectors is shown in Figure 11. In this figure I show the images of the reflectors for a constant angle of incidence of 45^0 (results for different angles of incidence as well as for different azimuths are shown later in the section). The wells are located on the two sides of the plot. The reflectors always intersect the wells at the correct depths but are pulled up because of our incorrect dip assumption.

The distortion of the shape of the reflectors can be qualitatively different if the reflectors dip out-of-plane. Depending on the azimuth of the reflector, either pull-

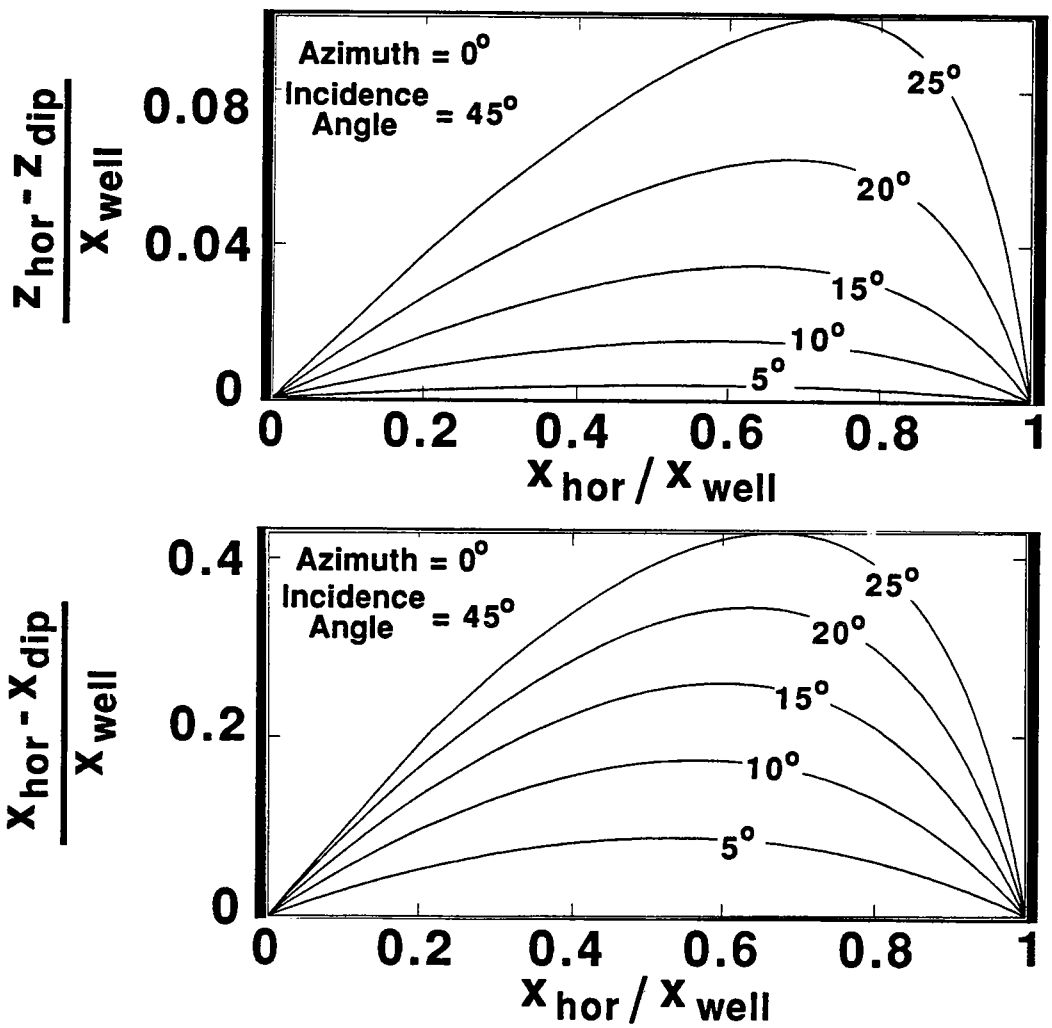

Figure 8: Vertical and lateral mispositioning of the reflection point for an in-plane dipping reflector.

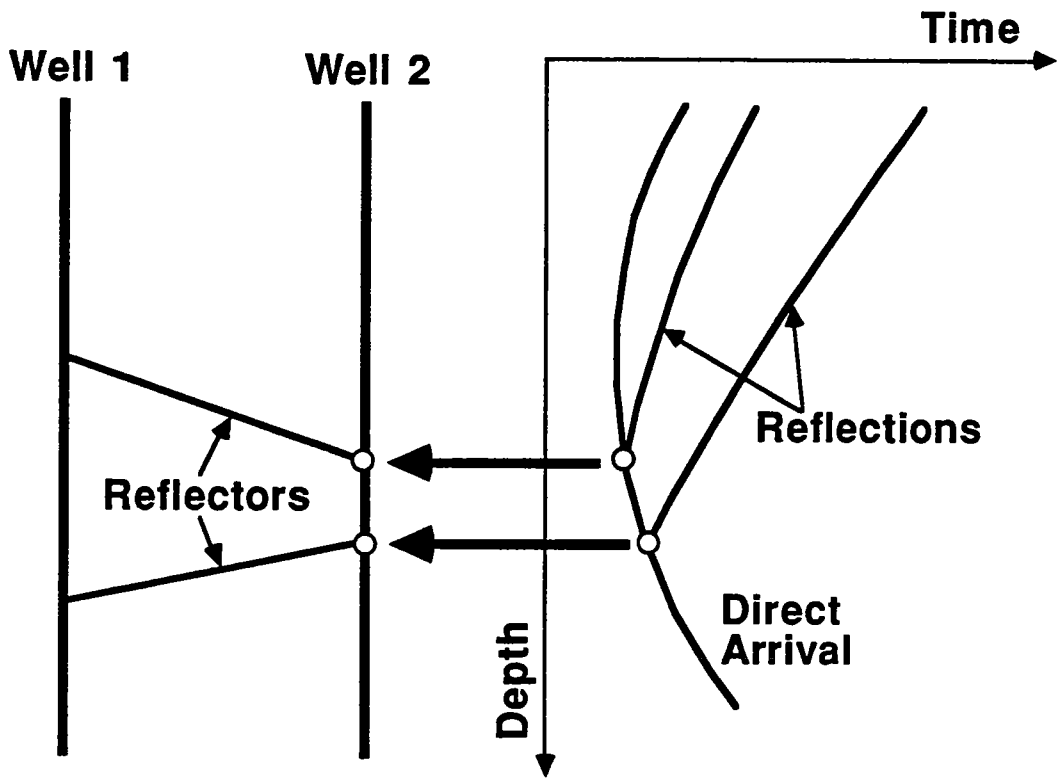

Figure 9: Reflection points at the wells are not mispositioned irrespective of dip. The intersections of the direct arrival with the reflection events correspond to reflection points at the wells and will always be mapped correctly.

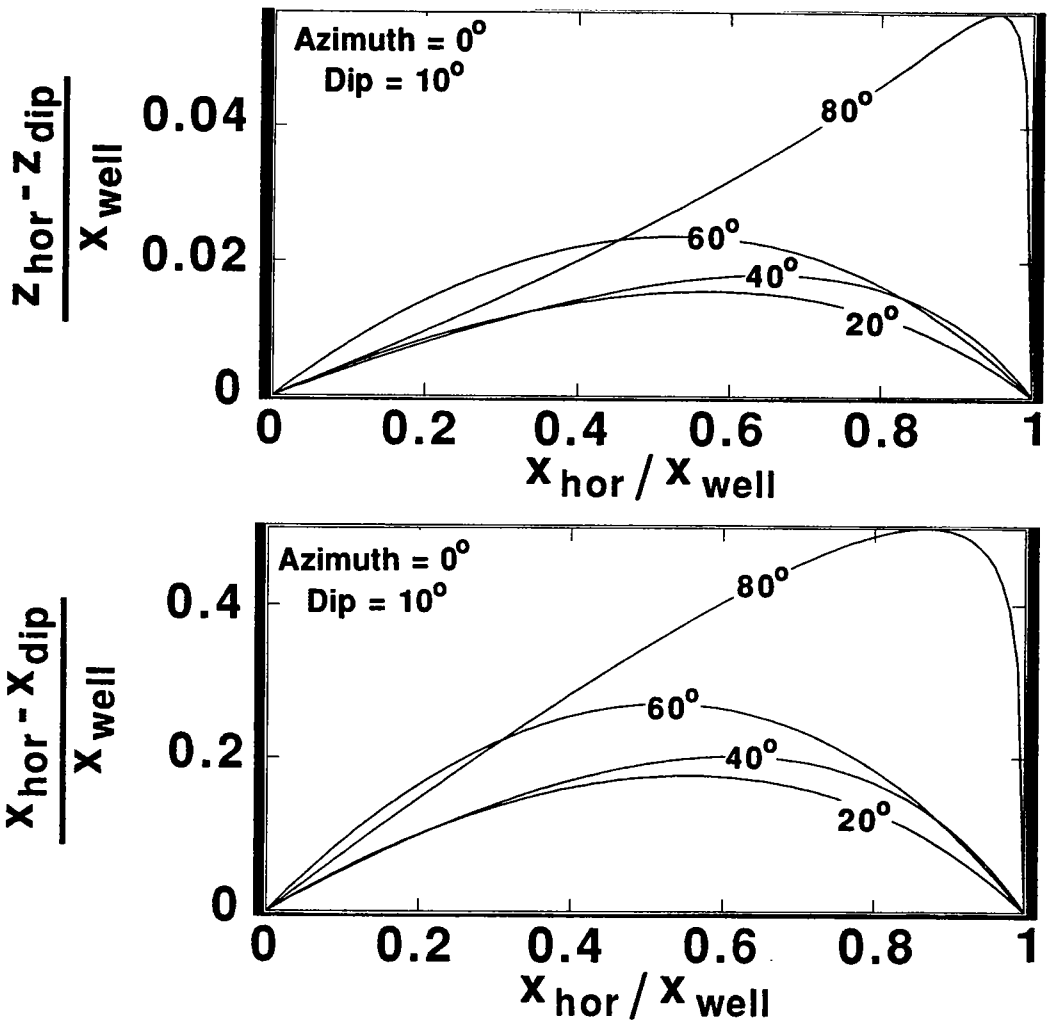

Figure 10: Vertical and lateral mispositioning of the reflection point for an in-plane dipping reflector (dip=10^0) and incidence angles ranging from 20^0 to 80^0.

ups or push-downs can be produced. This is illustrated in Figure 12, which shows the images of dipping reflectors with apparent in-plane dips ranging from 5^0 to 25^0. These are the dips of the intersection of the reflector plane with the well plane. The true maximum dips of these reflectors are related to the in-plane dips through the equation

$$\tan\theta_{in} = \tan\theta\cos\alpha \tag{10}$$

where θ_{in} is the in-plane dip, θ the maximum dip and α the azimuth.

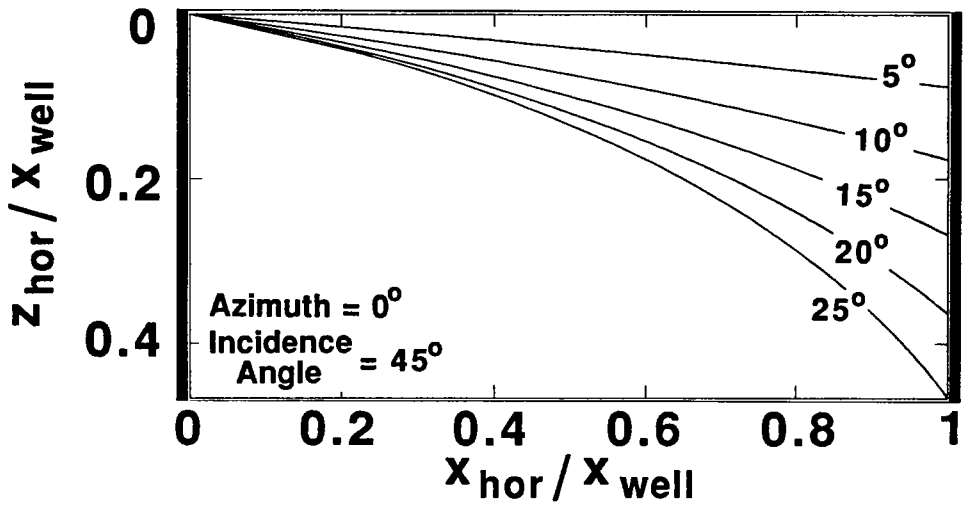

Figure 11: Images of in-plane dipping reflectors mapped with a horizontal-reflector algorithm. The true images of the reflectors are straight lines, connecting the intersections of the reflectors with the two wells.

As can be seen from this figure, for an azimuth of 45^0 the reflectors are pulled up, for an azimuth of 60^0 they have approximately the right shape and for an azimuth of 75^0 they are pushed down.

This example shows clearly that algorithms attempting to correctly image dipping reflectors should account for the azimuth of the reflector. This information cannot be determined from cross-well measurements in a single pair of wells. It will have to be estimated either through multiple cross-well surveys occupying several well pairs, or provided by other methods, like 3-D surface seismic. Notice that, in practice, even for the case of horizontal reflectors, the equivalent of out-of-plane dips can be created by well deviation.

Unlike vertical mispositioning, Figures 8 and 13 show that lateral mispositioning is not very sensitive to azimuth. This suggests that imaging algorithms designed for in-plane dipping reflectors would position events to an approximately correct horizontal location. Of course, the actual reflection point would be out of the well plane. The

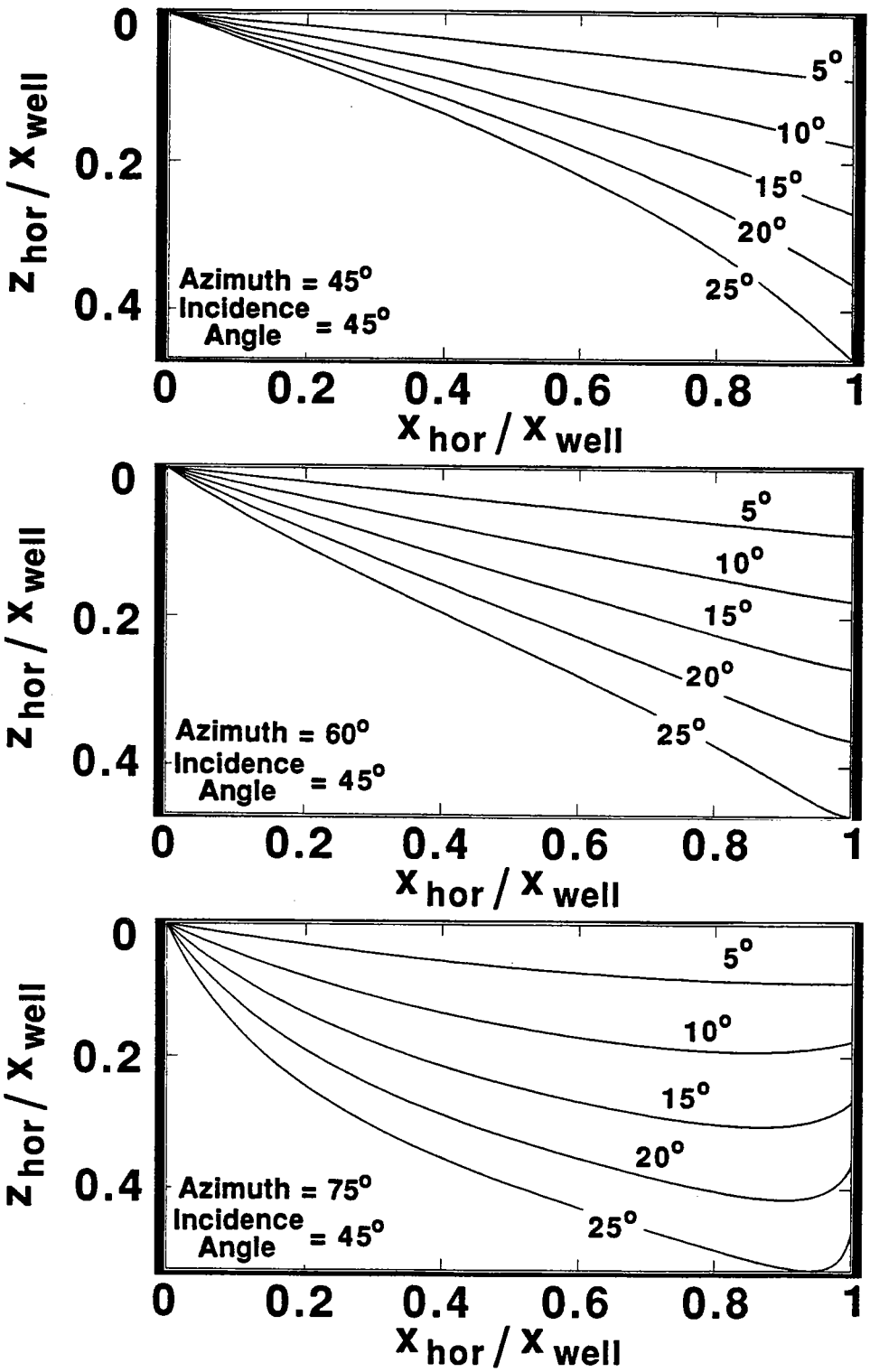

Figure 12: Images of out-of-plane dipping reflectors mapped with a horizontal-reflector algorithm for three different values of azimuth. The true in-plane images of the reflectors are straight lines, connecting the intersections of the reflectors with the two wells.

out-of-plane mispositioning of the reflection point $((y_{hor} - y_{dip})/x_{well})$ is shown in Figure 14. As expected it increases with increasing azimuth.

Figure 15 shows that, for larger incidence angles, the reflectors tend to be pulled up more. Lateral mispositioning also tends to increase as illustrated in Figure 16. On the other hand, out-of-plane mispositioning is reduced, since the isochrone ellipsoid gets more elongated with increasing angle of incidence. This is demonstrated in Figure 17.

VELOCITY SENSITIVITY

In this section we examine the sensitivity of the mapping to inaccuracies in the imaging velocity. We are going to consider the case of horizontal reflectors in a constant velocity model and study the lateral and vertical mispositioning of the reflection point when the imaging velocity is different from the true velocity.

The basic geometry is shown in Figure 18. Suppose the true reflection point is point A. As explained in an earlier section, point A will be located on a mapping trajectory corresponding to the particular source-receiver pair that is defined by the incidence angle ϕ and the horizontal location x. Suppose now we map the data with a velocity $v + \Delta v$ different from the correct value v. The data point that would map to point A will now map to point B along the same trajectory so that the total traveltime remains the same:

$$\frac{(SA) + (RA)}{v} = \frac{(SB) + (RB)}{v + \Delta v} \tag{11}$$

Suppose the coordinates of the true reflection point A are (x, z) and the coordinates of the mispositioned reflection point $(x - \Delta x, z - \Delta z)$. In Appendix B it is shown that the lateral and vertical mispositionings Δx and Δz normalized to the interwell distance x_{well} are given by the following expressions:

$$\frac{\Delta x}{x_{well}} = \frac{1}{2}[2(\frac{x}{x_{well}}) - 1](1 - \frac{1}{\sqrt{1 + \frac{(\frac{\Delta v}{v})^2 + 2(\frac{\Delta v}{v})}{\cos^2\phi}}}) \tag{12}$$

$$\frac{\Delta z}{x_{well}} = \frac{1}{2\tan\phi}(1 - \sqrt{1 + \frac{(\frac{\Delta v}{v})^2 + 2(\frac{\Delta v}{v})}{\cos^2\phi}}) \tag{13}$$

and for

$$\frac{1}{\cos^2\phi}(\frac{\Delta v}{v}) \ll 1 \tag{14}$$

which means small velocity error and small angles of incidence, we get the following simplified approximate expressions:

$$\frac{\Delta x}{x_{well}} \approx \frac{1}{2\cos^2\phi}[2(\frac{x}{x_{well}}) - 1](\frac{\Delta v}{v}) \tag{15}$$

$$\frac{\Delta z}{x_{well}} \approx -\frac{1}{\sin 2\phi}(\frac{\Delta v}{v}) \tag{16}$$

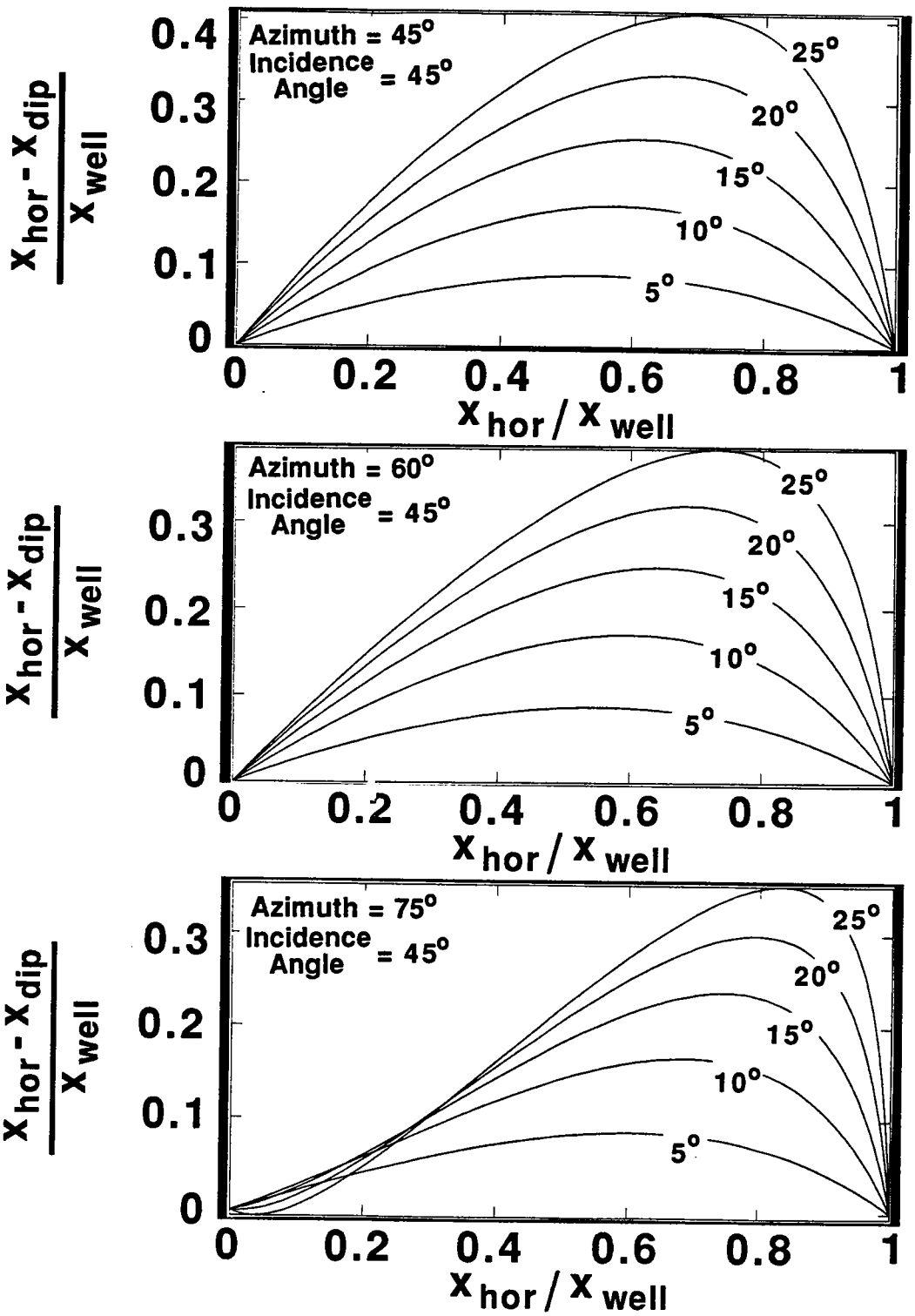

Figure 13: Lateral mispositioning of the reflection point for out-of-plane dipping reflectors for three different values of azimuth.

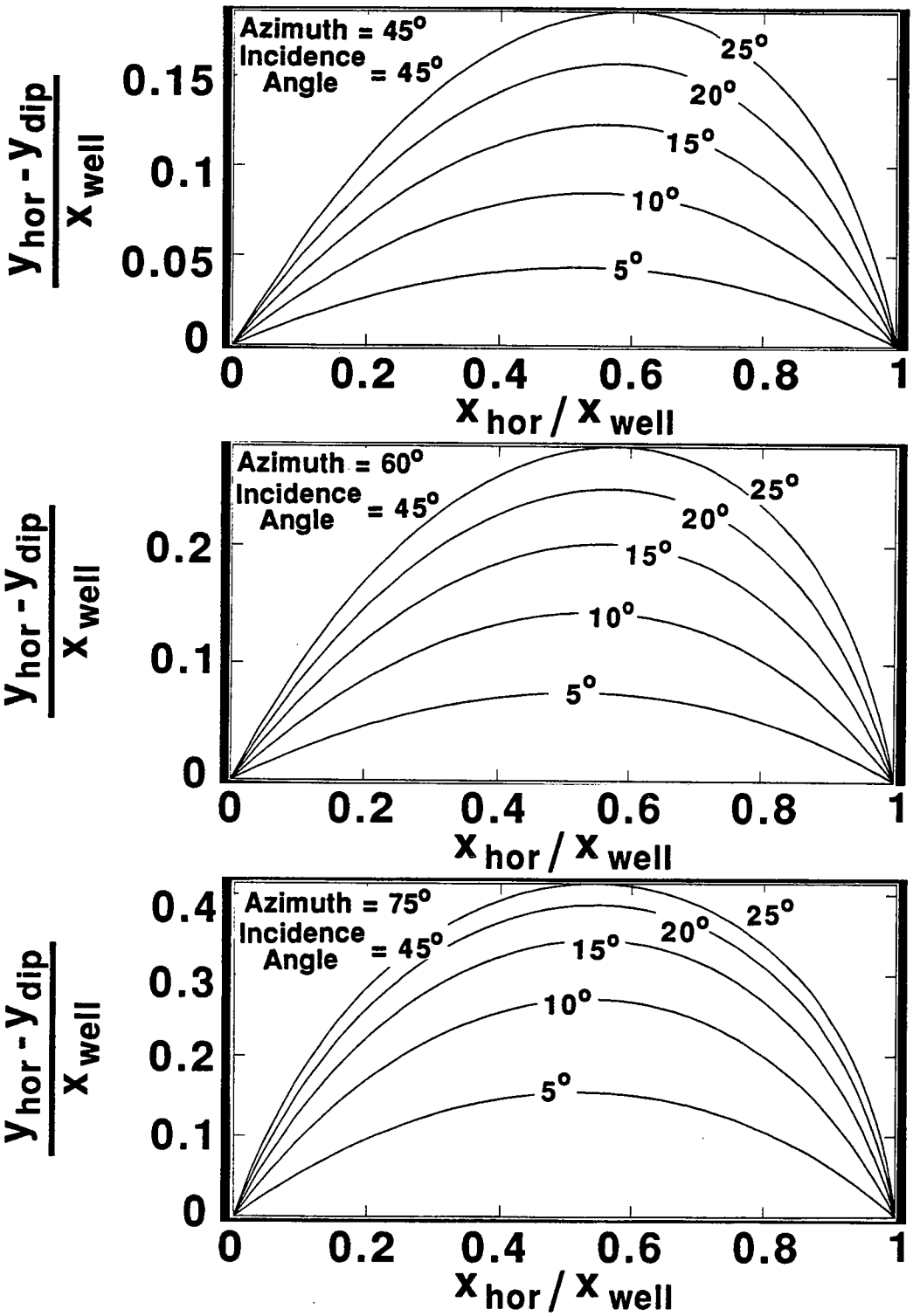

Figure 14: Out-of-plane mispositioning of the reflection point for out-of-plane dipping reflectors for three different values of azimuth.

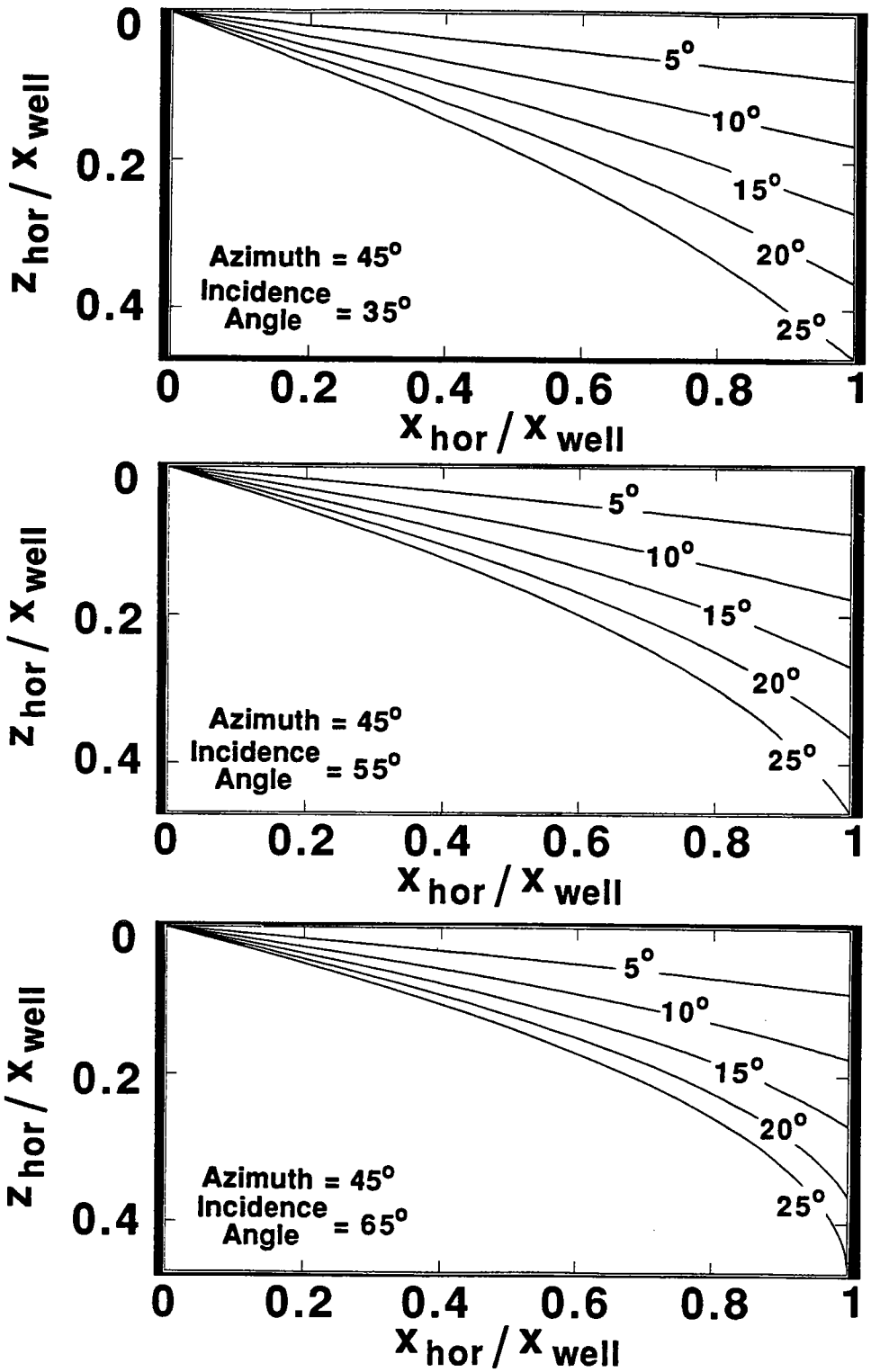

Figure 15: Images of out-of-plane dipping reflectors mapped with a horizontal-reflector algorithm for three different values of incidence angle. The true in-plane images of the reflectors are straight lines, connecting the intersections of the reflectors with the two wells.

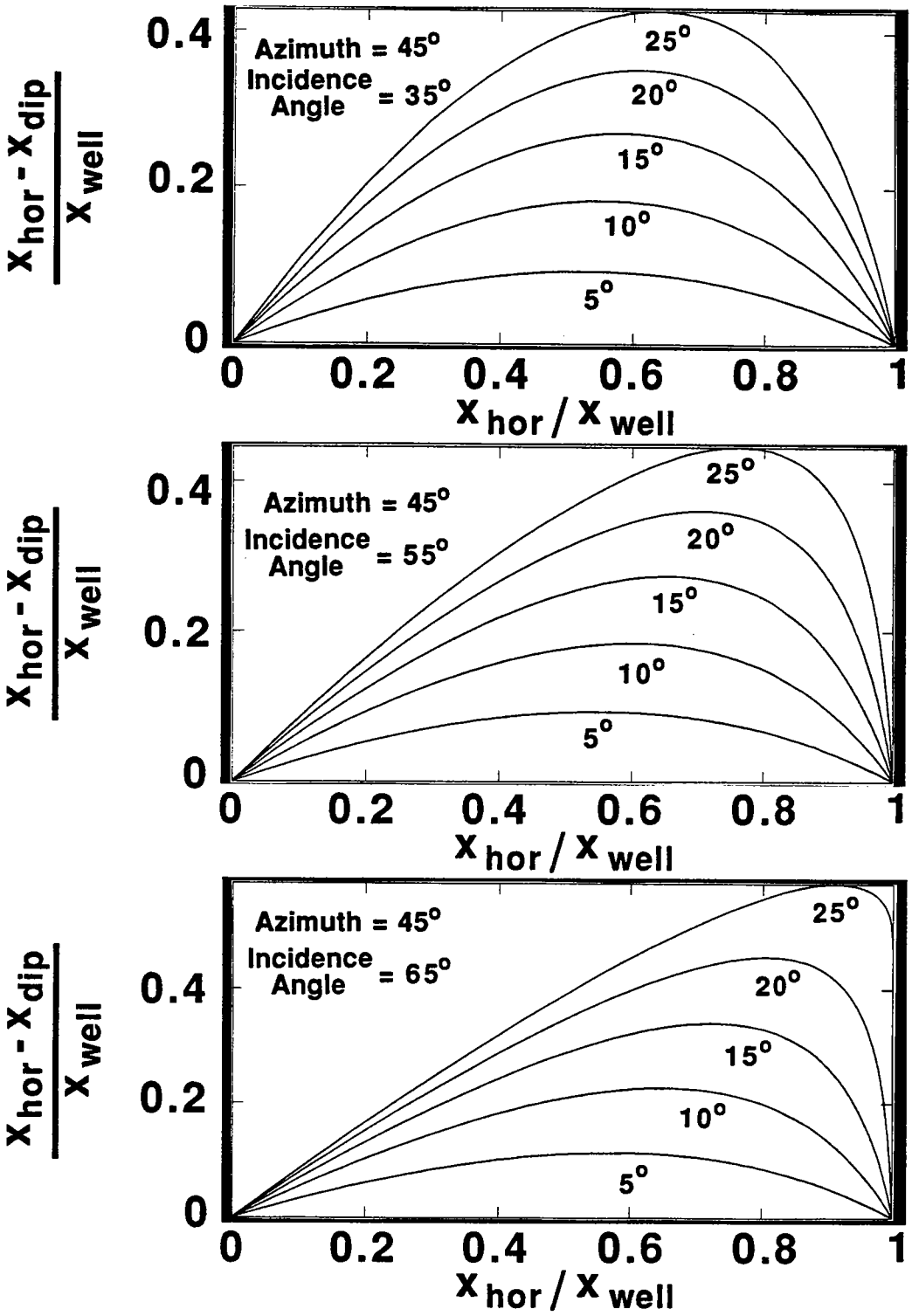

Figure 16: Lateral mispositioning of the reflection point for out-of-plane dipping reflectors for three different values of incidence angle.

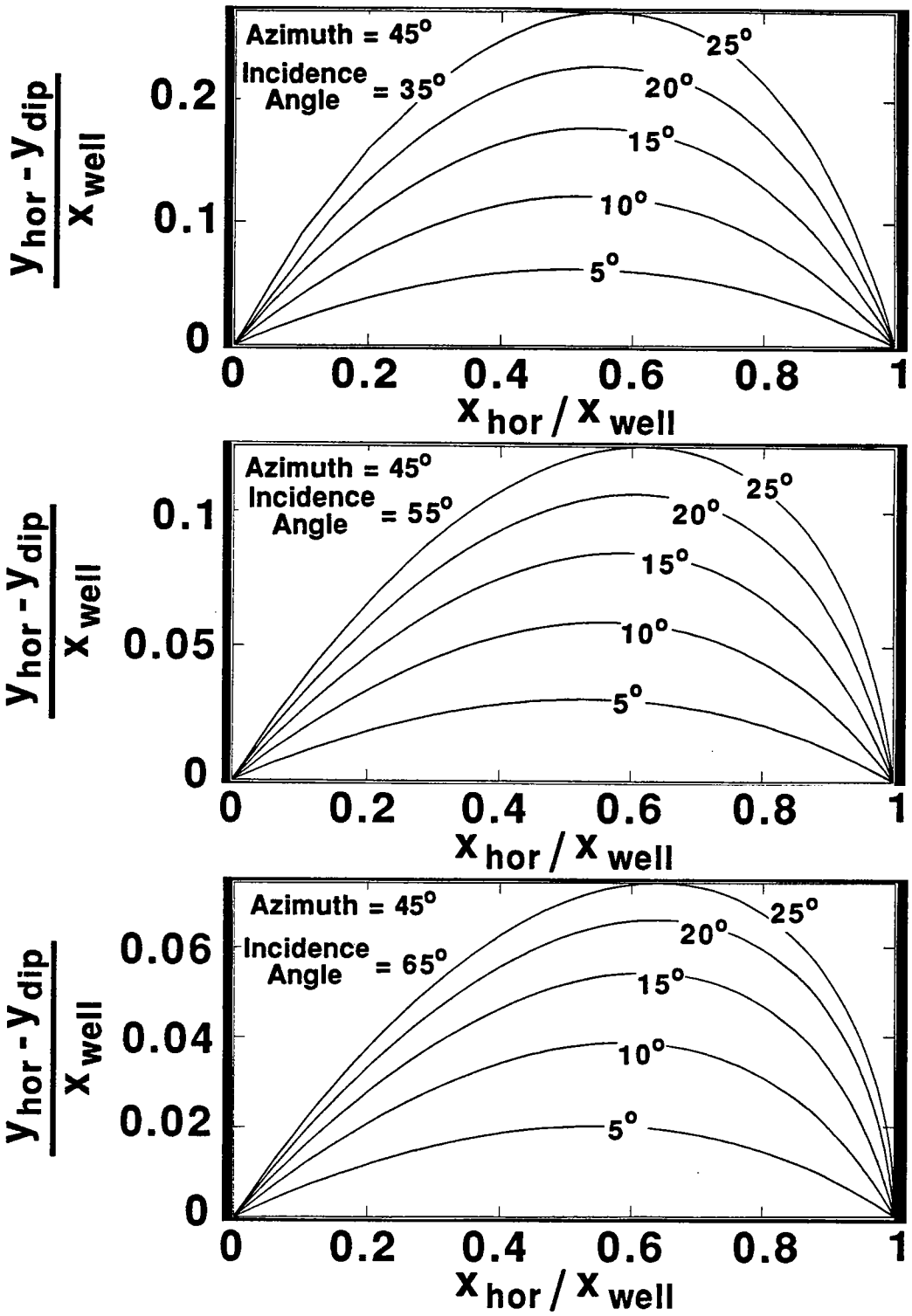

Figure 17: Out-of-plane mispositioning of the reflection point for out-of-plane dipping reflectors for three different values of incidence angle.

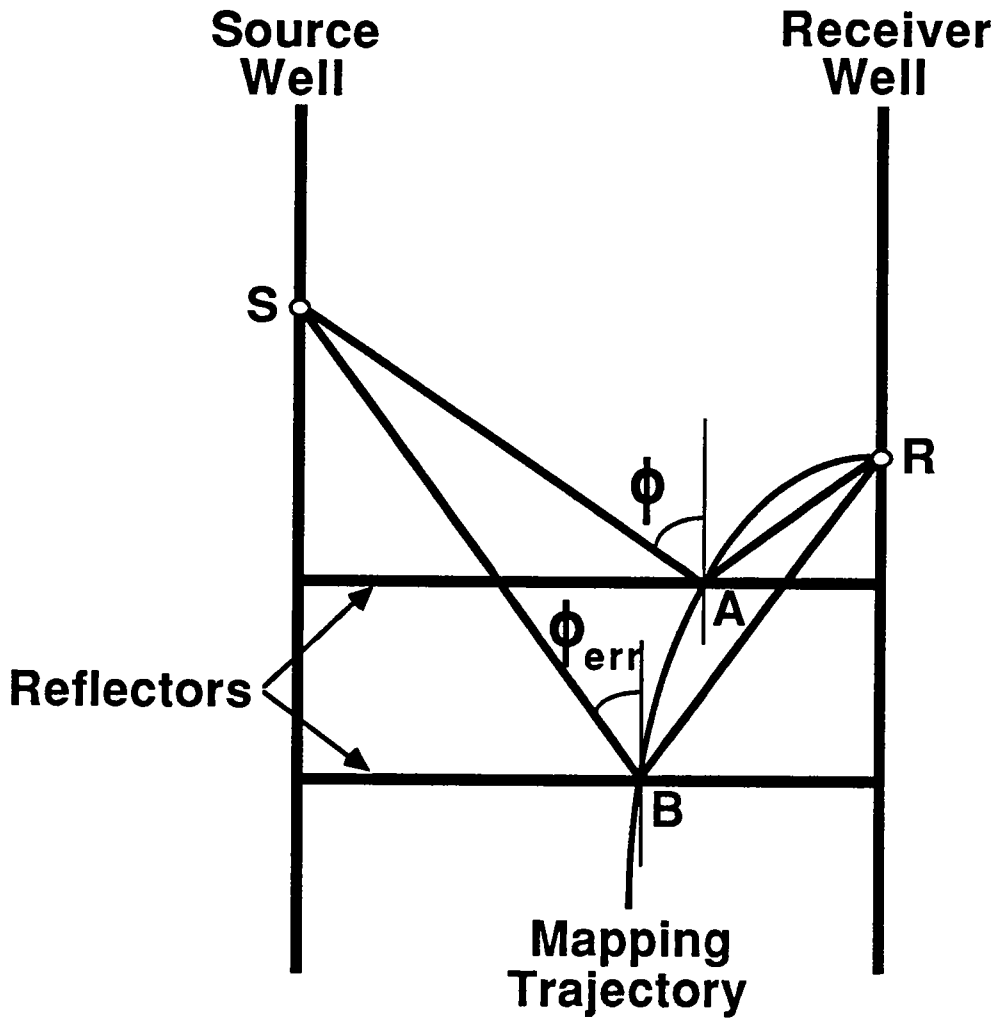

Figure 18: Mispositioning of the reflection point due to a wrong mapping velocity. A wrong mapping velocity will cause the data point that would map on point A to instead map on point B, along the same mapping trajectory, so that the total reflection traveltime remains constant.

Equations (12) and (13) show that mispositionings due to velocity inaccuracies depend on the amount of velocity error, expressed as a fraction of the true velocity, and scale with the interwell distance. Lateral mispositioning is largest for reflection points at the two wells and reduces to zero for reflection points located halfway between wells, because of the term $[2(x/x_{well}) - 1]$ in equation (12). Lateral mispositioning also increases with angle of incidence. These results can be explained by the shape of the mapping trajectories, shown in Figure 2. Large angles of incidence and reflection points close to the wells correspond to the flatter part of the trajectories. Since the reflection points move along the trajectories, reflection points located on the flatter parts will move laterally more than those located on the steeper parts. For reflection points located halfway between wells, the corresponding mapping trajectory is vertical, so the lateral mispositioning is zero. This situation is similar to the common-midpoint-gather geometry in surface seismic.

The effect of the angle of incidence on lateral and vertical mispositioning is shown in Figure 19. The curves shown there are plots of the quantities

$$\frac{\Delta x}{x_{well}[2(\frac{x}{x_{well}}) - 1]}, \frac{\Delta z}{x_{well}} \tag{17}$$

as functions of the angle of incidence, for velocity errors ranging from 1 to 15%. We can see that the vertical mispositioning is smallest for intermediate angles of incidence—around 45^0—as is suggested by the approximate expression in equation (16).

The angle of incidence in equations (12) and (13) is the angle of incidence for the correct location of the reflection point. As shown in Figure 18, when the reflection point moves, because of an error in velocity, the angle of incidence will also change to a new value ϕ_{err}. It is shown in Appendix B that

$$\tan\phi_{err} = \frac{\tan\phi}{\sqrt{1 + \frac{(\frac{\Delta v}{v})^2 + 2(\frac{\Delta v}{v})}{\cos^2\phi}}} \tag{18}$$

This equation can also be inverted to express ϕ as a function of ϕ_{err}. The result is

$$\tan\phi = \frac{(1 + \frac{\Delta v}{v})\tan\phi_{err}}{\sqrt{1 - [(\frac{\Delta v}{v})^2 + 2(\frac{\Delta v}{v})]\tan^2\phi_{err}}} \tag{19}$$

For small velocity error and small angles of incidence, we get approximately

$$\phi_{err} \approx \phi \tag{20}$$

In Figure 20 I plot the lateral and vertical mispositionings as functions of the erroneous angle of incidence ϕ_{err}. The terminations of the curves correspond to the values of ϕ_{err} for which the argument of the square root in the denominator of equation (19) becomes negative. Physically, this corresponds to the case when the real angle of

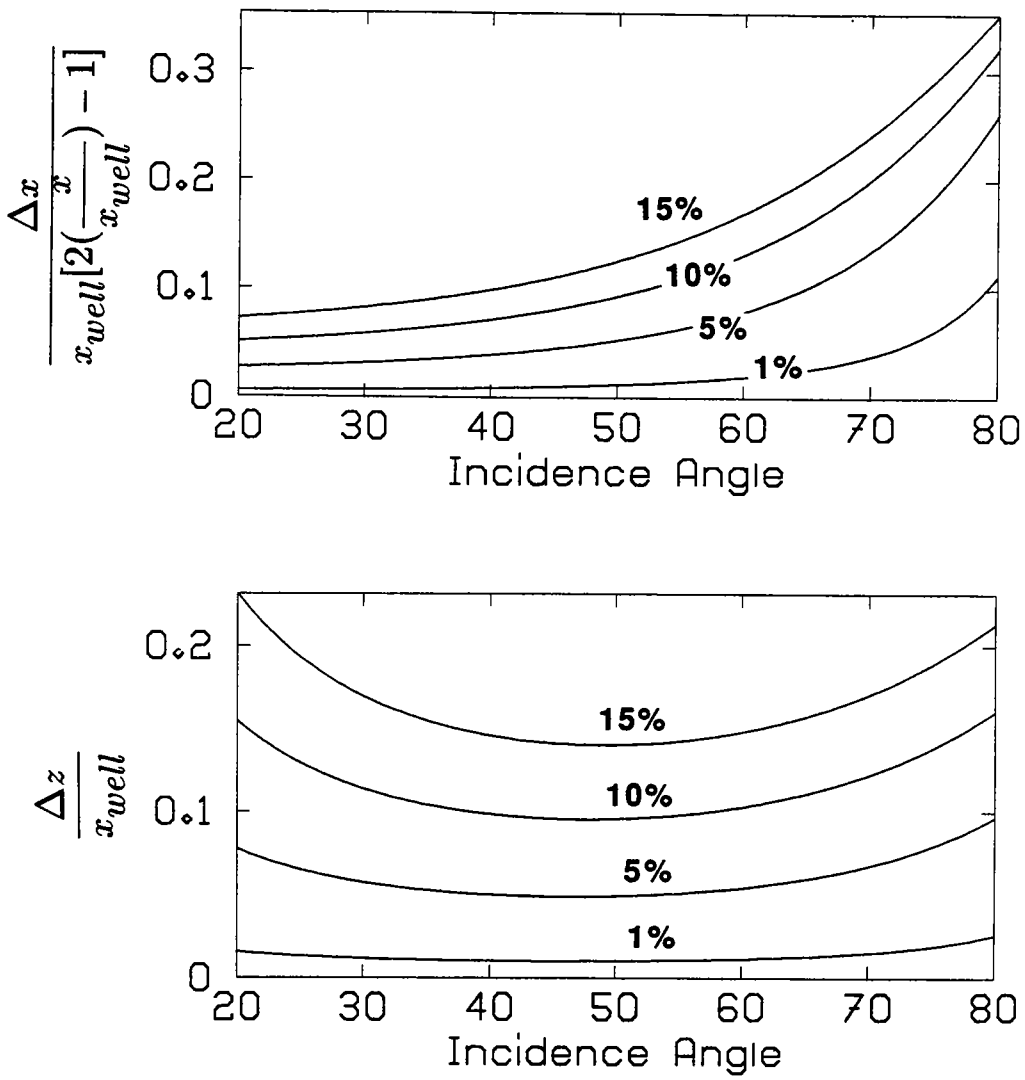

Figure 19: Lateral and vertical mispositionings of the reflection point due to a wrong mapping velocity plotted as functions of the incidence angle.

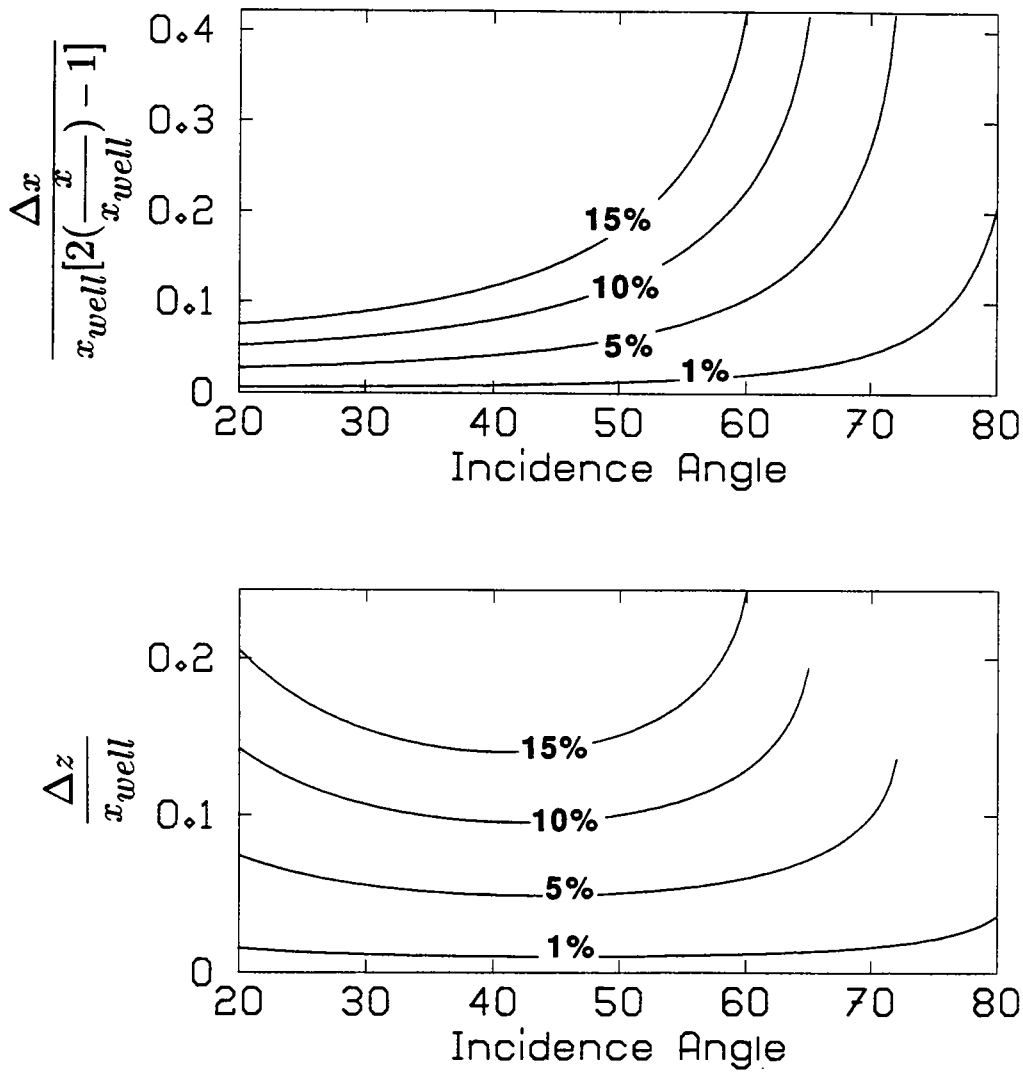

Figure 20: Lateral and vertical mispositionings of the reflection point due to a wrong mapping velocity, plotted as functions of the erroneous incidence angle.

incidence ϕ is equal to 90^0. Notice the large values of mispositioning for large angles of incidence. For angles larger than about 55^0 to 60^0, lateral mispositioning is much larger than vertical mispositioning.

The vertical mispositioning curves in Figure 20, produced from equations (12), (13) and (19) represent the moveouts of the events that we would observe, if we mapped the data with the wrong velocity. Equations (12), (13) and (19) could potentially be used for velocity analysis.

The results in this section can serve as a guide to help us determine the accuracy we need in our estimate of the velocity, in order to stack cross-well reflections. Assuming that mispositioning by more than a certain fraction of the wavelength produces an unacceptable stack, equations (12) and (13) imply that the necessary accuracy depends on the ratio of the interwell distance over the wavelength—since mispositionings are proportional to the interwell distance. So, if the distance between wells is equivalent to a larger number of wavelengths, we need a more accurate velocity to produce a good stack. The accuracy also depends on the range of incidence angles over which we want to stack. Intermediate angles of incidence (40^0-55^0) are less sensitive to velocity than very small or very large angles of incidence. For large angles of incidence, the lateral location of the reflection point is extremely sensitive to velocity.

ANALYSIS OF THE STRETCH CAUSED BY MAPPING

The VSP-CDP mapping algorithm maps traces to curvilinear trajectories like the ones shown in Figure 2. Consequently it introduces distortions to the signal's waveform similar to the stretch associated with the normal moveout (NMO) correction. Since the trajectories are not vertical, the VSP-CDP mapping produces both a vertical and a horizontal stretch. In the case of NMO the stretch is only vertical.

This stretch needs to be understood, because it lengthens waveforms in both the vertical and the horizontal direction and, therefore, it limits both vertical and horizontal resolution. An analysis of the stretch produced by the mapping is presented in this section.

The mapping is not a stationary operation: the stretch of the wavelet changes with time. Therefore, a convenient way of analyzing it is through the use of instantaneous attributes (instantaneous frequency, phase and wavenumber). This approach was introduced by Barnes (1992) as a way of analyzing the NMO stretch.

An infinitesimal segment of a trace at time t comprises a phase change $d\theta$ occurring over a time interval dt. The VSP-CDP algorithm maps this trace segment to a location in space, characterized by the horizontal space coordinate x and depth z. Now the phase change $d\theta$ occurs over a vertical distance dz and a horizontal distance dx. A definition of instantaneous phase can be found in Yilmaz (1987, p.521). Instantaneous frequency is defined as

$$\omega(t) = \frac{d\theta(t)}{dt} \tag{21}$$

Similarly, instantaneous horizontal and vertical wavenumbers are defined as

$$k_x(x,z) = \frac{d\theta(x,z)}{dx} \tag{22}$$

$$k_z(x,z) = \frac{d\theta(x,z)}{dz} \tag{23}$$

The last two equations can be written as

$$k_x = \frac{d\theta}{dt}\frac{dt}{dx} = \omega\frac{dt}{dx} \tag{24}$$

$$k_z = \frac{d\theta}{dt}\frac{dt}{dz} = \omega\frac{dt}{dz} \tag{25}$$

For the constant velocity case, it can be easily shown (see Figure 21) that

$$x = \frac{1}{2}x_{well}\left(1 + \frac{z_R - z_S}{\sqrt{v^2t^2 - x_{well}^2}}\right) \tag{26}$$

$$z = \frac{1}{2}\left[(z_S + z_R) + \sqrt{v^2t^2 - x_{well}^2}\right] \tag{27}$$

where x_{well} is the interwell distance, z_S and z_R the source and receiver depths and v the velocity.

Based on equation (26) and the geometry shown in Figure 21, it can be shown that

$$\frac{dx}{dt} = -\frac{1}{2}\frac{x_{well}(z_R - z_S)v^2t}{\left(\sqrt{v^2t^2 - x_{well}^2}\right)^3} = -\frac{v\tan^2\phi}{2\cos\phi\tan\phi_0} \tag{28}$$

where ϕ is the angle of incidence and ϕ_0 is the angle between the vertical and the line connecting source and receiver. In Appendix C it is shown that

$$\frac{\tan\phi}{\tan\phi_0} = 2(\frac{x}{x_{well}}) - 1 \tag{29}$$

so

$$\frac{dx}{dt} = \frac{v\tan\phi}{2\cos\phi}[1 - 2(\frac{x}{x_{well}})] \tag{30}$$

Also from equation (27) it can be shown that

$$\frac{dz}{dt} = \frac{v^2t}{2\sqrt{v^2t^2 - x_{well}^2}} = \frac{v}{2\cos\phi} \tag{31}$$

So, finally

$$k_x = \frac{2}{1 - 2(\frac{x}{x_{well}})}\frac{\omega}{v}\frac{\cos\phi}{\tan\phi} \tag{32}$$

$$k_z = 2\frac{\omega}{v}\cos\phi \tag{33}$$

The last two equations determine how the temporal spectrum of the trace is transformed to spatial spectra as the result of the mapping. It can be shown that the amplitude spectrum transformation is

$$A_x(k_x) = |1 - 2(\frac{x}{x_{well}})|\,\frac{v\tan\phi}{2\cos\phi}\,A_t\left([1 - 2(\frac{x}{x_{well}})]\,\frac{vk_x\tan\phi}{2\cos\phi}\right) \tag{34}$$

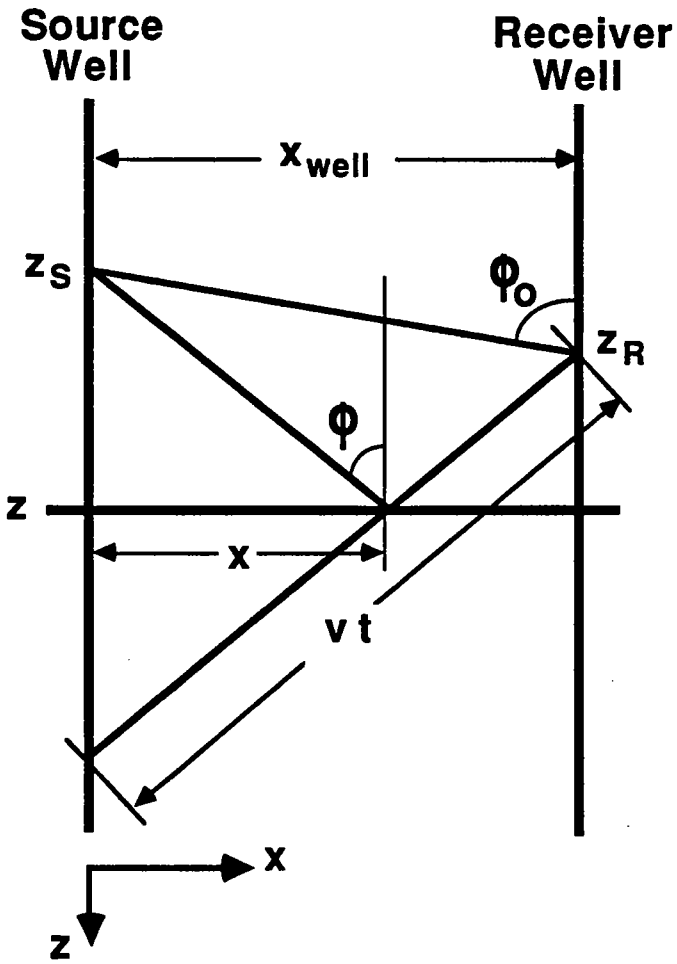

Figure 21: Basic crosswell reflection geometry.

$$A_z(k_z) = \frac{v}{2\cos\phi} A_t\left(\frac{vk_z}{2\cos\phi}\right) \tag{35}$$

where A_t is the temporal spectrum, A_x the horizontal spectrum and A_z the depth spectrum. The proof is similar to the one given in Barnes (1992) for the NMO stretch.

The meaning of the above equations is explained schematically in Figure 22. A band-limited time wavelet produces, after mapping, a band-limited depth wavelet and a band-limited horizontal wavelet. Given a time wavelet, the depth wavelet after mapping depends on the velocity and the angle of incidence. As the angle of incidence increases, its cosine decreases and the energy in the depth spectrum moves towards lower wavenumbers (larger wavelengths). This means that, for larger angles of incidence we get more vertical stretch.

The horizontal wavelet after mapping depends on the velocity, the angle of incidence and the horizontal location of the reflection point. As the angle of incidence increases, its cosine and inverse tangent decrease and the energy in the horizontal spectrum moves towards lower wavenumbers (larger wavelengths), producing larger horizontal stretch. Horizontal stretch also increases as the quantity $|1 - 2(\frac{x}{x_{well}})|$ increases. This means that the horizontal stretch is larger for reflection points close to the two wells and decreases as the reflection points move towards the middle. For reflection points halfway between wells, k_x goes to infinity, hence the horizontal wavelength produced by horizontal stretch goes to zero. This means that for reflection points halfway between wells we get no horizontal stretch. This can easily be explained by the shape of the mapping trajectories in Figure 2. We get more horizontal stretch on the parts of the trajectories that are closer to the horizontal. As we move from the wells towards the middle, the trajectories become more vertical. For reflection points halfway between wells, the trajectories are exactly vertical, which means no horizontal stretch.

Equations (32) and (33) can also be written as expressions for the effective horizontal and vertical wavelengths after mapping:

$$\lambda_x = [1 - 2(\frac{x}{x_{well}})]\frac{\lambda}{2}\frac{\tan\phi}{\cos\phi} \tag{36}$$

$$\lambda_z = \frac{\lambda}{2\cos\phi} \tag{37}$$

In the above equations λ is the wavelength $2\pi v/\omega$. The effective horizontal wavelength due to stretch for reflection points at the well and a wavelength equal to 1 is shown in Figure 23.

Equations (36) and (37) as well as Figure 23 demonstrate that the use of wide angles of incidence for imaging produces large horizontal and vertical stretch and loss of both lateral and vertical resolution.

FRESNEL ZONES

A popular way of quantifying the lateral resolution of reflection imaging has been via the use of the concept of Fresnel zones. The first Fresnel zone is defined as the

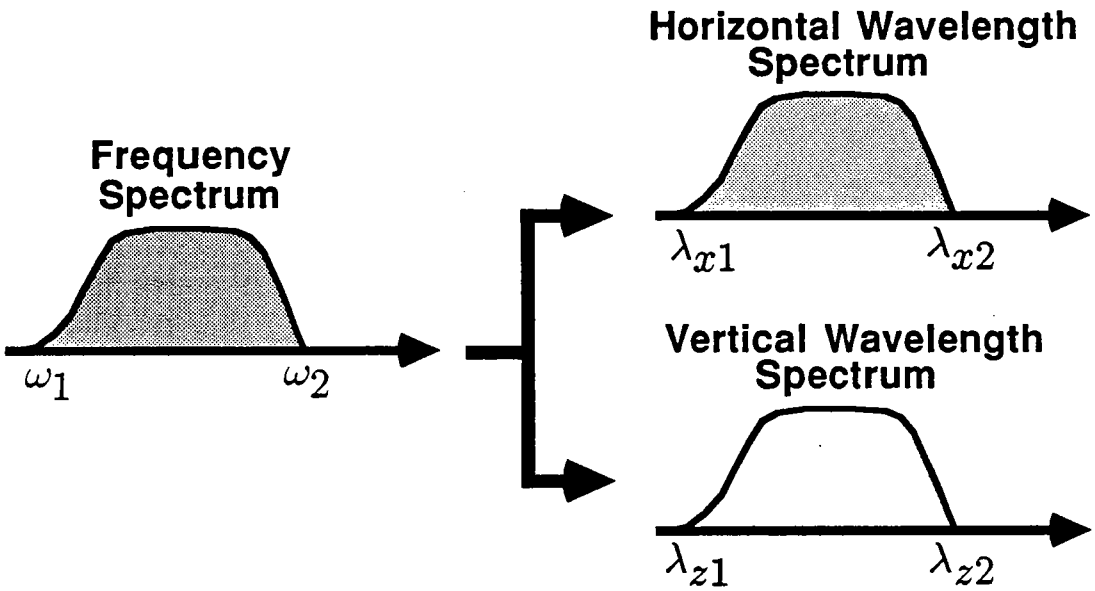

$$\lambda_{x1} = [1 - 2(\frac{x}{x_{well}})]\frac{\pi v}{\omega_1}\frac{\tan\phi}{\cos\phi}$$

$$\lambda_{x2} = [1 - 2(\frac{x}{x_{well}})]\frac{\pi v}{\omega_2}\frac{\tan\phi}{\cos\phi}$$

$$\lambda_{z1} = \frac{\pi v}{\omega_1 \cos\phi}$$

$$\lambda_{z2} = \frac{\pi v}{\omega_2 \cos\phi}$$

Figure 22: Transformation of the time spectrum to horizontal and vertical spectra.

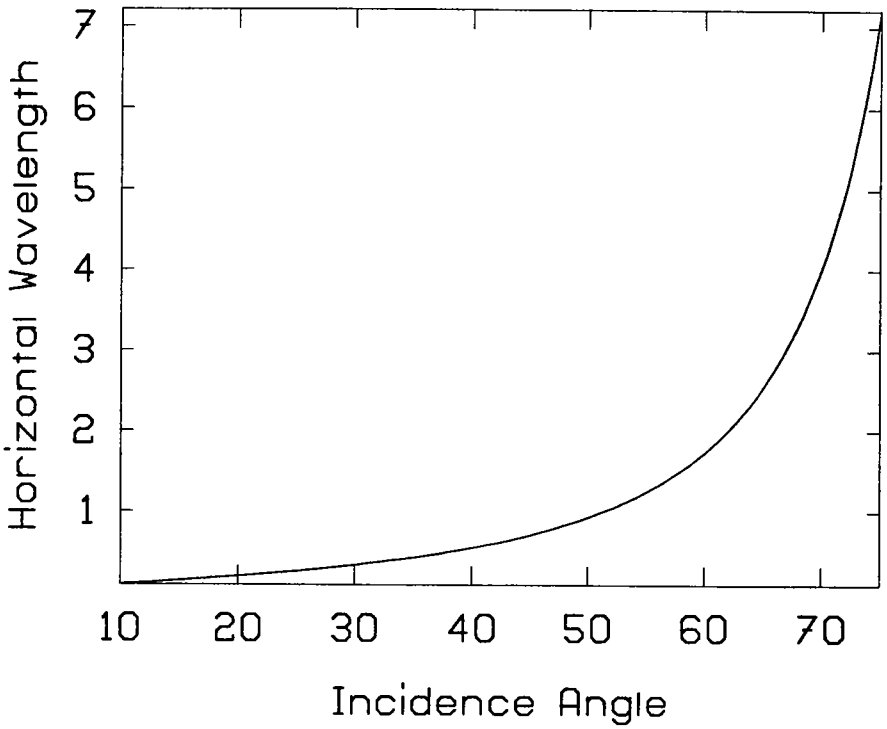

Figure 23: Horizontal wavelength due to stretch for reflection points at the well (wavelength=1).

region of constructive interference enclosing the ray-theoretic reflection point. It is the part of the reflector for which the traveltime difference between the specular reflection and the non-specular arrivals is less than half the dominant period (Sheriff, 1980).

Since the VSP-CDP mapping is a ray-theoretic imaging algorithm, mapping reflection data to their corresponding specular reflection points, Fresnel zones are an appropriate way to quantify its lateral resolution. It is important to make clear though that the Fresnel zones do not represent the theoretical limit of lateral resolution that can be achieved with crosswell reflection imaging. Lateral resolution can be improved through the procedure of migration. It has been shown (Berkhout, 1984; Claerbout, 1984) that migration collapses the Fresnel zone to a much narrower focus, whose lateral dimension depends on the horizontal wavenumber spectrum that can be reconstructed from the data given the particular recording geometry. It has been shown (Devaney, 1984; Harris, 1987) that, for infinite recording aperture, the smaller horizontal wavelength that can be reconstructed from the crosswell geometry is equal to the wavelength of the seismic waves used for imaging and it increases as the aperture is reduced.

Fresnel zones have to be examined in 3-D. Interference that affects the reflection response will not only come from scatterers located in the interwell plane but also from scatterers outside the plane (see Figure 24). In surface seismic, 3-D recording allows the use of 3-D migration to collapse the Fresnel zone. For the crosswell geometry, with sources and receivers mainly in a plane, the out-of-plane interference cannot be eliminated.

In the following we calculate the in-plane and out-of-plane sizes of the Fresnel zone for the crosswell geometry. We assume a simple model of horizontal reflectors in a constant velocity model.

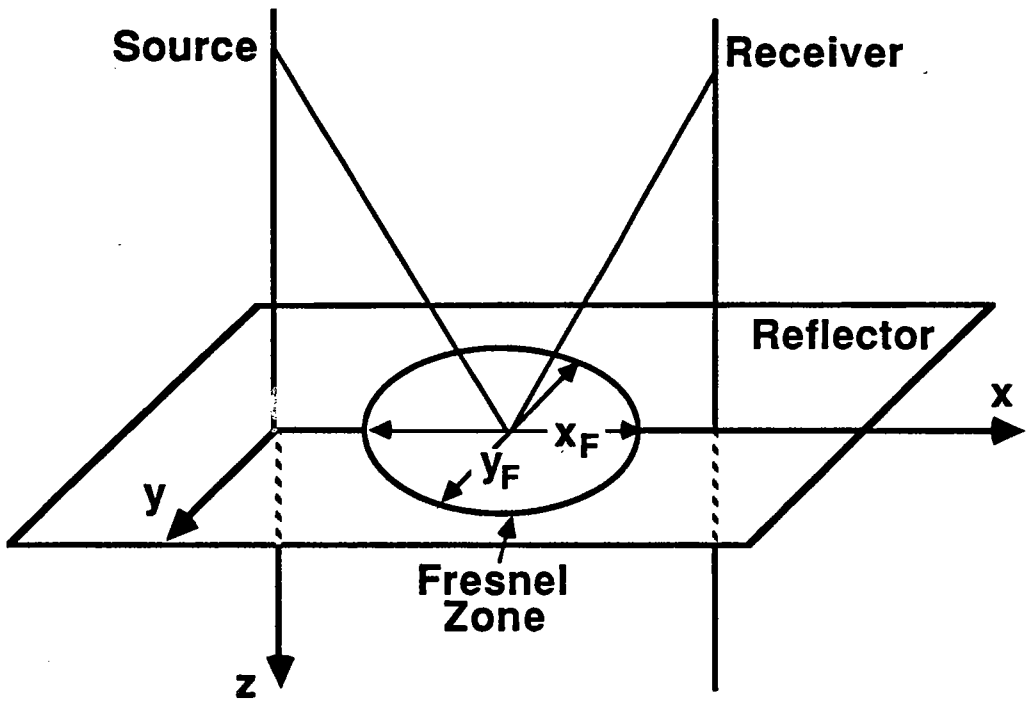

Figure 24: Fresnel zone.

The basic geometry for the calculation of the in-plane size of the Fresnel zone is shown in Figure 25. Suppose the specular reflection point is point A and that the traveltime for the reflection from this point is t. Then, point A is the point at which the isochrone ellipse corresponding to time t is tangent to the horizontal reflector on which A is located.

The isochrone ellipse corresponding to time $t + T/2$, where T is the dominant period, intersects the horizontal reflector at points B and C. According to the definition given before, the in-plane size of the Fresnel zone is the length of the segment BC. The calculations are described in Appendix D. The final result is

$$\frac{x_F}{x_{well}} = \frac{2\sqrt{B^2 - AC}}{A \sin \phi_0} \tag{38}$$

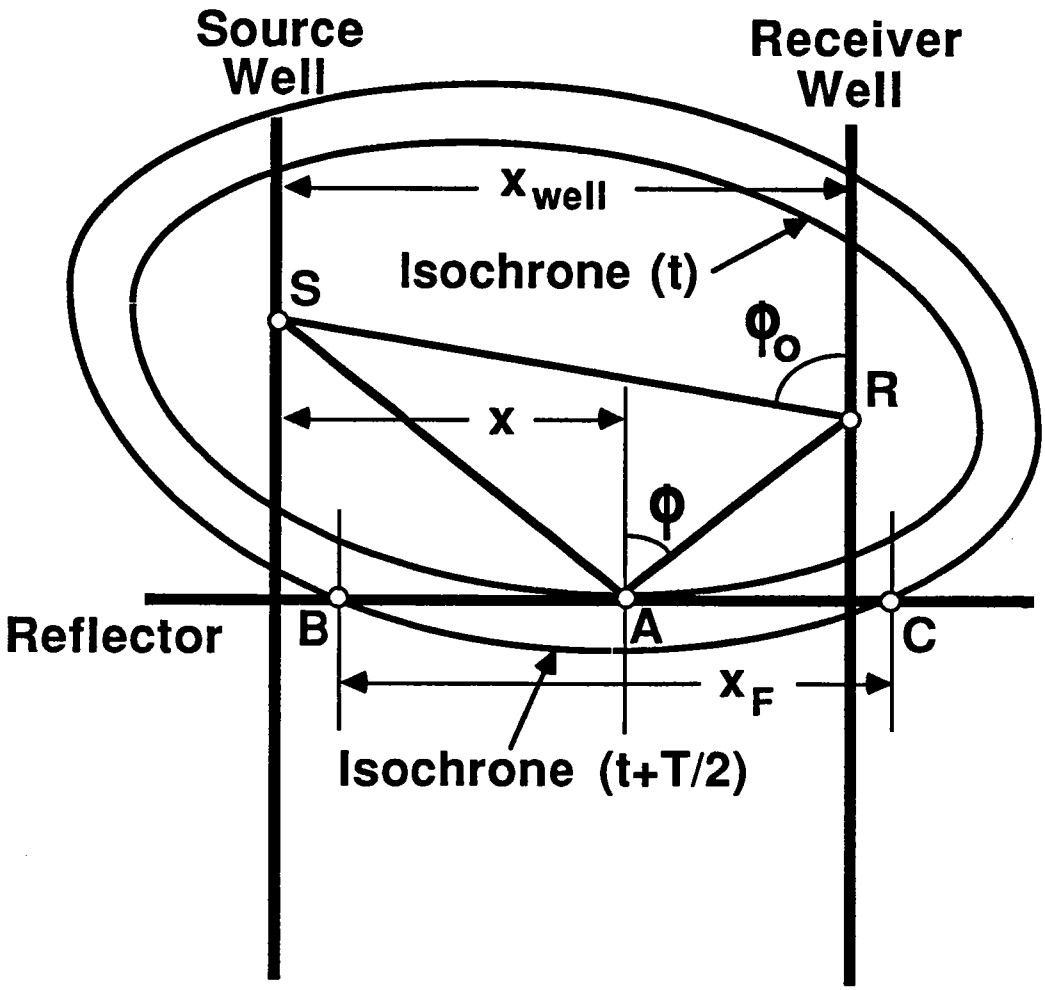

Figure 25: Basic geometry for in-plane Fresnel zone calculation.

where

$$A = \frac{1}{a^2} + \frac{1}{b^2 \tan^2 \phi_0} \tag{39}$$

$$B = \frac{1}{2b^2 \sin \phi_0 \tan \phi_0 \tan \phi} \tag{40}$$

$$C = \frac{1}{4b^2 \sin^2 \phi_0 \tan^2 \phi} - 1 \tag{41}$$

$$a = \frac{1}{2 \sin \phi} + \frac{\lambda_0}{4} \tag{42}$$

$$b = \frac{1}{2}\sqrt{\frac{\lambda_0^2}{4} + \frac{\lambda_0}{\sin \phi} + \frac{1}{\sin^2 \phi} - \frac{1}{\sin^2 \phi_0}} \tag{43}$$

In the above equations x_F is the in-plane size of the Fresnel zone, x_{well} the interwell distance, ϕ the angle of incidence and λ_0 the wavelength expressed as a fraction of the interwell distance

$$\lambda_0 = \frac{\lambda}{x_{well}} \tag{44}$$

where λ is the wavelength. As shown in Figure 25, ϕ_0 is the angle formed by the source-receiver raypath and the vertical. This angle can be calculated from the incidence angle ϕ and the horizontal location of the reflection point x, through the equation

$$\tan \phi_0 = \frac{\tan \phi}{2(\frac{x}{x_{well}}) - 1} \tag{45}$$

Equations (38) to (45) show that the in-plane size of the Fresnel zone for the crosswell geometry scales with the interwell distance.

The in-plane size of the Fresnel zone as a fraction of the interwell distance is plotted in Figure 26 as a function of the horizontal location of the reflection point and for angles of incidence ranging from 35^0 to 75^0. The wavelength was assumed to be one fiftieth (0.02) of the interwell distance. From this figure we can see that the in-plane size of the Fresnel zone is smaller close to the two wells and increases as we move towards the middle. Its maximum is halfway between wells.

Angle of incidence significantly affects the in-plane size of the Fresnel zone. Larger angles of incidence produce larger in-plane Fresnel zones. For an angle of incidence of 65^0 the in-plane size of the Fresnel zone halfway between wells is larger than one-third the interwell distance for this particular choice of wavelength-to-interwell-distance ratio (0.02). Even for an angle of incidence of 35^0, we get a Fresnel zone larger than one-fifth the interwell distance. For an interwell distance of 500 ft and a wavelength of 10 ft, the in-plane size of the Fresnel zone halfway between wells ranges between about 100 ft for an angle of incidence of 35^0 to about 250 ft for an angle of incidence of 75^0.

The method of calculation of the size of the out-of-plane Fresnel zone is similar to the one used for the in-plane case. The boundary of the Fresnel zone in 3-D can be calculated as the intersection of the isochrone ellipsoid for time $t + T/2$ with the

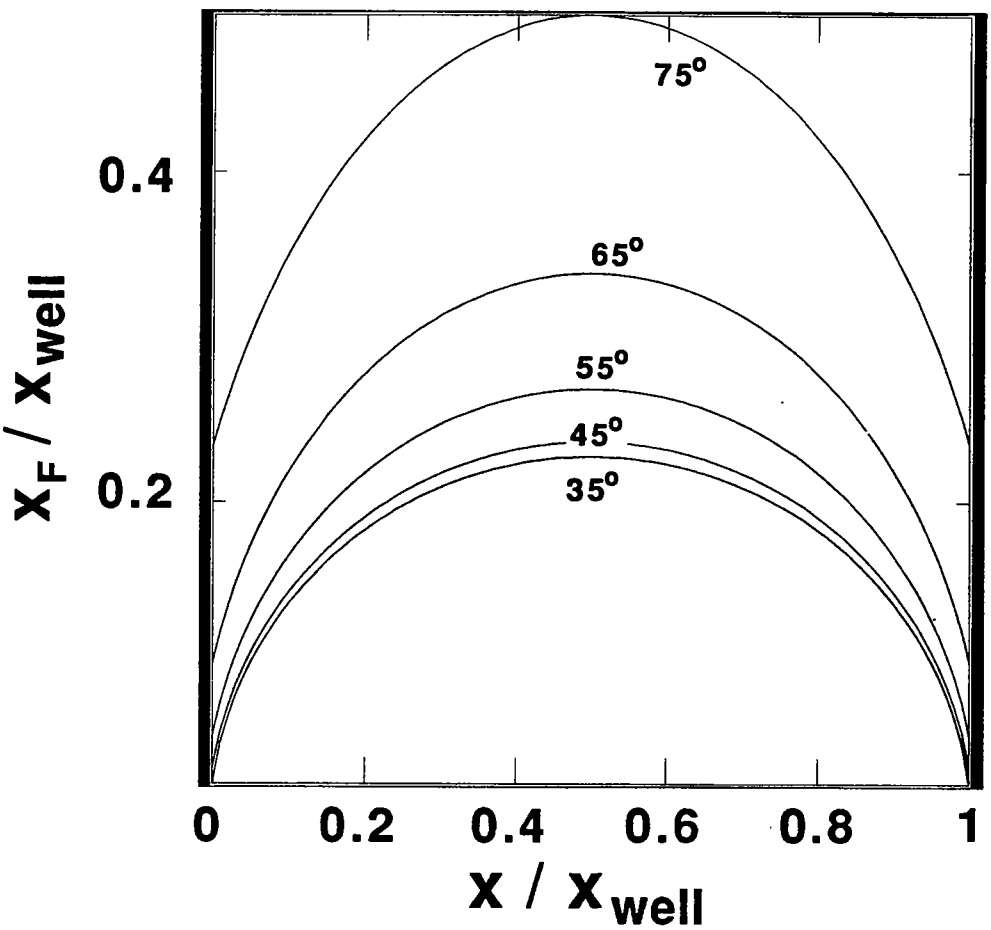

Figure 26: In-plane size of Fresnel zone.

reflector plane. Here, as out-of-plane size of the Fresnel zone, we define its dimension in the direction perpendicular to the interwell plane and for the horizontal location of the reflection point (see Figure 24). The calculations are performed in Appendix D. The final result is

$$\frac{y_F}{x_{well}} = 2b\left[1 - \frac{1}{a^2}\left(\frac{\sin\phi_0\tan\phi + \cos\phi_0}{\tan\phi_w} - \frac{1}{2\sin\phi_0}\right)^2 - \frac{1}{b^2}\left(\frac{\sin\phi_0 - \cos\phi_0\tan\phi}{\tan\phi_w}\right)^2\right]^{1/2} \tag{46}$$

In the above expression y_F is the out-of-plane size of the Fresnel zone. The quantities x_{well}, a, b, ϕ, ϕ_0 have been defined before. The angle ϕ_w is defined through the equation

$$\frac{1}{\tan\phi_w} = \frac{1}{2}\left(\frac{1}{\tan\phi} + \frac{1}{\tan\phi_0}\right) \tag{47}$$

Similar to the in-plane case, the out-of-plane size of the Fresnel zone scales with the interwell distance.

The out-of-plane size of the Fresnel zone as a fraction of the interwell distance is plotted in Figure 27 as a function of the horizontal location of the reflection point and for angles of incidence ranging from 35^0 to 75^0. The wavelength was again assumed to be one fiftieth of the interwell distance. Similar to the in-plane case, the out-of-plane size of the Fresnel zone is smaller close to the two wells and increases as we move towards the middle. Unlike the in-plane case, it decreases with angle of incidence. For an interwell distance of 500 ft and a wavelength of 10 ft, the out-of-plane size of the Fresnel zone halfway between wells ranges between about 70 and 100 ft.

CONCLUSIONS

In this paper a number of issues associated with the reflector mapping algorithm were studied. The more important conclusions are given below.

Dipping reflectors

- Mispositioning due to dip scales with the interwell distance and does not depend on velocity.
- Independent of the real dip and real azimuth and the dip and azimuth assumed by the imaging algorithm, reflection points at the wells will be mapped at their correct location. This suggests that, if the dip is constant between wells, one could first map assuming horizontal reflectors, estimate the dip from the intersections of the reflectors with the wells and, in a second pass, image with an algorithm that assumes the correct dip.
- Lateral mispositioning is larger than vertical mispositioning.
- When imaged with a horizontal-reflector algorithm, in-plane dipping reflectors are pulled up between wells.
- When imaged with a horizontal-reflector algorithm, out-of-plane dipping reflectors can be either pulled up or pulled down. In the absence of out-of-plane

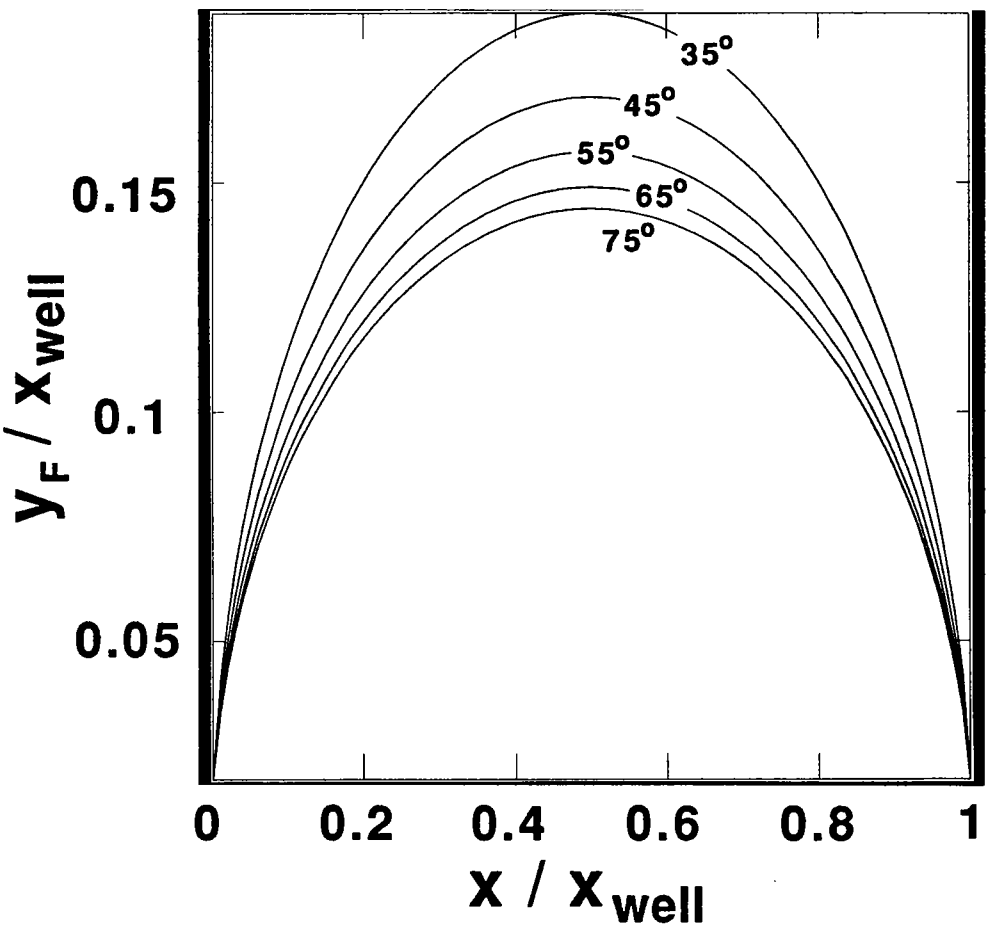

Figure 27: Out-of-plane size of Fresnel zone.

measurements, it might be difficult to separate such distortions from inaccuracies in the velocity model.

- Lateral mispositioning is not very sensitive to the azimuth of the reflector. This suggests that imaging algorithms designed for in-plane dipping reflectors would position reflection points to an approximately correct horizontal location.
- Reflector pull-ups and lateral mispositioning tend to increase with angle of incidence.
- For wider angles of incidence, the true reflection points for out-of-plane dipping reflectors are closer to the interwell plane.

Velocity

- Mispositionings due to velocity inaccuracies depend on the percentage of velocity error, not on its absolute value.
- Both vertical and lateral mispositionings scale with the interwell distance.
- Vertical mispositioning is smallest for intermediate angles and increases for small or large angles. It does not depend on the horizontal location of the reflection point.
- Lateral mispositioning is largest for reflection points close to the wells and decreases to zero for reflection points located halfway between wells.
- As the ratio of interwell distance over wavelength increases, a more accurate velocity is needed to stack crosswell reflections.

Stretch

- Both vertical and lateral stretches increase with angle of incidence.
- Vertical stretch is independent of the location of the reflection point. Lateral stretch is largest close to the wells and decreases as we move towards the middle.
- Loss of resolution due to stretch depends on the wavelength and is independent of the interwell distance.

Fresnel zones

- The size of the Fresnel zone (both in-plane and out-of-plane) scales with the interwell distance.
- The in-plane size of the Fresnel zone increases with increasing incidence angle.
- The out-of-plane size of the Fresnel zone decreases with increasing incidence angle.

- Fresnel zones of a few hundred feet should be expected for typical interwell distances and wavelengths.

REFERENCES

Abdalla, A. A., Stewart, R. R., and Henley, D. C., 1990, Traveltime inversion and reflection processing of cross-hole seismic data: Expanded abstracts of the 60th Ann. Internat. Mtg., Soc. Expl. Geophys., 47-50.

Baker, L. J., and Harris, J. M., 1984, Cross-borehole seismic imaging: Expanded abstracts of the 54th Ann. Internat. Mtg., Soc. Expl. Geophys., 23-25.

Barnes, A. E., 1992, Another look at NMO stretch: Geophysics **57**, 749-751

Berkhout, A. J., 1984, Seismic resolution: Resolving power of acoustical echo techniques: Geophysical Press, London - Amsterdam, 95-146.

Beydoun, W. B., Delvaux, J., Mendes, M., Noual, G., and Tarantola, A., 1988, Practical aspects of an elastic migration/inversion of crosshole data for reservoir characterization: a Paris basin example: Geophysics **54**, 1587-1595.

Beydoun, W. B., and Mendes, M., 1989, Elastic ray-Born l2-migration/inversion: Geophys. J., **97**, 151-160.

Claerbout, J. F., 1984, Imaging the Earth's Interior, Blackwell Scientific Publications, Palo Alto, 18-20.

Devaney, A. J., 1984, Geophysical diffraction tomography: IEEE Trans. Geosci. Remote Sensing, GE-**22**, 3-13.

Harris, J. M., 1987, Diffraction tomography with arrays of discrete sources and receivers: IEEE Trans. Geosci. Remote Sensing, GE-**25**, 448-455.

Hu, L., McMechan, G. A., and Harris, J. M., 1988, Acoustic prestack migration of cross-hole data: Geophysics **53**, 1015-1023.

Iverson, W. P., 1988, Crosswell logging for acoustic impedance: J. Pet. Tech., **40**, 75-82.

Lazaratos, S. K., Rector, J. W., Harris, J. M., and Van Schaack, M., 1991, High resolution imaging with crosswell reflection data: Presented at the 61st Ann. Internat. Mtg., Soc. Expl. Geophys., 107-110.

Lazaratos, S. K., Rector, J. W., Harris, J. M., and Van Schaack, M., 1992, High resolution cross well imaging of a West Texas carbonate reservoir: Presented at the 62nd Ann. Internat. Mtg., Soc. Expl. Geophys., 49-53.

Lo, T. W., Toksöz, M. N., Xu, S., and Wu, R. S., 1988, Ultrasonic laboratory tests of geophysical tomographic reconstruction: Geophysics, **53**, 947-956

Luo, Y., and Schuster, G. T., 1990, Wave-equation traveltime + waveform inversion: Presented at the 60th Ann. Internat. Mtg., Soc. Expl. Geophys., 1223-1225.

Miller, D., Oristaglio, M., and Beylkin, G., 1987, A new slant on seismic imaging: Migration and integral geometry: Geophysics, **52**, 943-964.

Pratt, R. G., and Worthington, M. H., 1990, Inverse theory applied to multi-source cross-hole tomography. Part 1: Acoustic wave-equation method: Geophysical Prospecting, **38**, 287-310.

Pratt, R. G., and Worthington, M. H., 1990, Inverse theory applied to multi-source cross-hole tomography. Part 2: Elastic wave-equation method: Geophysical Prospecting, **38**, 311-329.

Sheriff, R. E., 1980, Nomogram for Fresnel-zone calculation: Geophysics, **45**, 968-972.

Woodward, M. J., 1989, Wave-equation tomography: Ph.D. thesis, Stanford Univ. pp.73.

Wu, R. S., and Toksöz, M. N., 1987, Diffraction tomography and multisource holography applied to seismic imaging: Geophysics, **52**, 11-25.

Wyatt, K. D., and Wyatt, S. B., 1981, Determination of subsurface structural information using the vertical seismic profile: Expanded abstracts of the 51st Ann. Internat. Mtg., Soc. Expl. Geophys., 1915-1949.

Yilmaz, Ö, 1987, Seismic data processing: Investigations in Geophysics, Vol. 2, Soc. Expl. Geophys., Tulsa, p.521.

APPENDIX A - MISPOSITIONING CAUSED BY DIP

In this appendix I sketch the derivation of equations (1) to (8), describing the mispositioning of the reflection point, caused by dip.

The basic geometry is shown in Figure A.1. We work in two different coordinate systems. The first—the xyz coordinate system—has its origin on the source; the x axis is horizontal, the z axis vertical and the y axis perpendicular to the plane defined by the wells. The second—the $x'y'z'$ coordinate system—has its origin in the middle of the linear segment connecting source and receiver; the x' axis is parallel to that segment, the z' axis is perpendicular to it and the y' axis is perpendicular to the interwell plane.

The transformation that relates the xyz and $x'y'z'$ coordinates is

$$\begin{bmatrix} x \\ y \\ z \end{bmatrix} = \begin{bmatrix} \sin\phi_0 & 0 & -\cos\phi_0 \\ 0 & 1 & 0 \\ \cos\phi_0 & 0 & \sin\phi_0 \end{bmatrix} \begin{bmatrix} x' \\ y' \\ z' \end{bmatrix} + \begin{bmatrix} \frac{x_{well}}{2} \\ 0 \\ \frac{x_{well}}{2\tan\phi_0} \end{bmatrix} \tag{48}$$

The equation of the dipping reflector in the xyz coordinate system is

$$x\sin\theta\cos\alpha + y\sin\theta\sin\alpha - z\cos\theta = d \tag{49}$$

where θ the dip, α the azimuth of the reflector (see Figure 6) and d the distance of the reflector plane from the origin of the xyz coordinate system. In the $x'y'z'$ coordinate system this equation becomes:

$$x'(\sin\phi_0\sin\theta\cos\alpha - \cos\phi_0\cos\theta) + y'\sin\theta\sin\alpha - z'(\sin\phi_0\cos\theta + \cos\phi_0\sin\theta\cos\alpha)$$

$$+ \frac{x_{well}}{2}\sin\theta\cos\alpha - \frac{x_{well}}{2\tan\phi_0}\cos\theta = d \tag{50}$$

This last equation gives

$$\frac{dz'}{dx'} = \frac{\sin\phi_0\sin\theta\cos\alpha - \cos\phi_0\cos\theta}{\sin\phi_0\cos\theta + \cos\phi_0\sin\theta\cos\alpha} \tag{51}$$

$$\frac{dz'}{dy'} = \frac{\sin\theta\sin\alpha}{\sin\phi_0\cos\theta + \cos\phi_0\sin\theta\cos\alpha} \tag{52}$$

The equation of the isochrone ellipsoid (this ellipsoid is the locus of points such that the total traveltime for a wave travelling from the source to any point on the ellipsoid and from that point to the receiver is constant) in the coordinate system $x'y'z'$ is

$$(\frac{x'}{a})^2 + (\frac{y'}{b})^2 + (\frac{z'}{b})^2 = 1 \tag{53}$$

where

$$a = \frac{vt}{2} = \frac{x_{well}}{2\sin\phi} \tag{54}$$

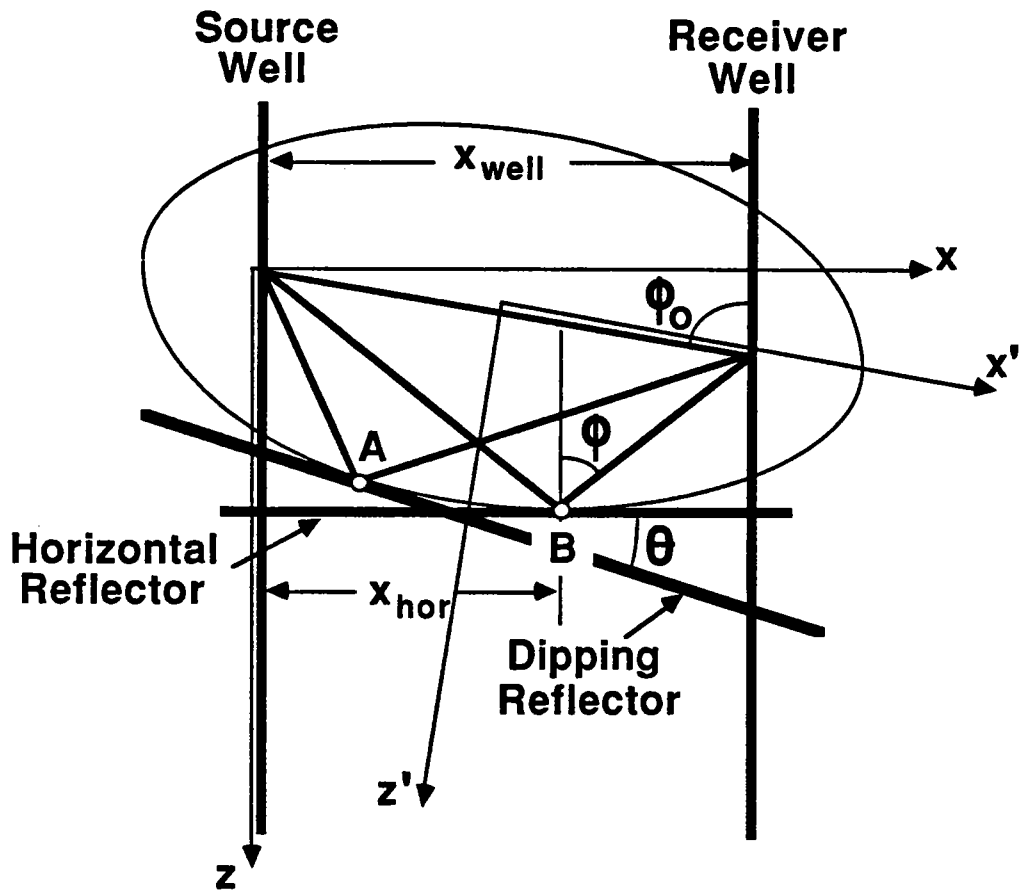

Figure A.1: Reflection point mispositioning due to dip.

$$b = \frac{1}{2}\sqrt{(vt)^2 - (\frac{x_{well}}{\sin\phi_0})^2} = \frac{x_{well}}{2\sin\phi\sin\phi_0}\sqrt{\sin^2\phi_0 - \sin^2\phi} \tag{55}$$

The tangent plane to this isochrone ellipsoid at the point $(x'_{dip}, y'_{dip}, z'_{dip})$ is described by the equation

$$\frac{x'_{dip}x'}{a^2} + \frac{y'_{dip}y'}{b^2} + \frac{z'_{dip}z'}{b^2} = 1 \tag{56}$$

which gives

$$\frac{dz'}{dx'} = -\frac{x'_{dip}}{z'_{dip}}\frac{b^2}{a^2} \tag{57}$$

$$\frac{dz'}{dy'} = -\frac{y'_{dip}}{z'_{dip}} \tag{58}$$

We want to find a point $(x'_{dip}, y'_{dip}, z'_{dip})$ on the isochrone ellipsoid, at which the dipping reflector, defined by equation (50), is tangent to the ellipsoid. For this point to lie on the ellipsoid, it has to satisfy equation (53). So:

$$(\frac{x'_{dip}}{a})^2 + (\frac{y'_{dip}}{b})^2 + (\frac{z'_{dip}}{b})^2 = 1 \tag{59}$$

Also, in order for the tangent of the ellipsoid to coincide with the reflector plane, we need to have, according to equations (51), (52), (57) and (58)

$$-\frac{x'_{dip}}{z'_{dip}}\frac{b^2}{a^2} = \frac{\sin\phi_0\sin\theta\cos\alpha - \cos\phi_0\cos\theta}{\sin\phi_0\cos\theta + \cos\phi_0\sin\theta\cos\alpha} \tag{60}$$

$$-\frac{y'_{dip}}{z'_{dip}} = \frac{\sin\theta\sin\alpha}{\sin\phi_0\cos\theta + \cos\phi_0\sin\theta\cos\alpha} \tag{61}$$

The last three equations can be solved for the coordinates $x'_{dip}, y'_{dip}, z'_{dip}$. The solution is

$$x'_{dip} = \frac{a^2\lambda_1}{\sqrt{a^2\lambda_1^2 + b^2(\lambda_2^2 + \lambda_3^2)}} \tag{62}$$

$$y'_{dip} = -\frac{b^2\lambda_2}{\sqrt{a^2\lambda_1^2 + b^2(\lambda_2^2 + \lambda_3^2)}} \tag{63}$$

$$z'_{dip} = \frac{b^2\lambda_3}{\sqrt{a^2\lambda_1^2 + b^2(\lambda_2^2 + \lambda_3^2)}} \tag{64}$$

where λ_1, λ_2 and λ_3 are the quantities defined by equations (6), (7) and (8). Rotating back to the xyz coordinate system, using the definitions of a and b (equations (54) and (55)), equation (9) (proved in Appendix C) and also the fact that

$$z_{hor} = \frac{x_{hor}}{\tan\phi} \tag{65}$$

we end up with equations (1) to (8).

APPENDIX B - MISPOSITIONING CAUSED BY ERRONEOUS IMAGING VELOCITY

In this appendix I describe the derivation of equations (12), (13) and (18). The basic geometry is shown in Figure B.1. Point B lies on the isochrone ellipse, described by the equation

$$(\frac{x'}{a})^2 + (\frac{z'}{b})^2 = 1 \tag{66}$$

where

$$a = \frac{(v + \Delta v)t}{2} \tag{67}$$

$$b = \frac{1}{2}\sqrt{(v + \Delta v)^2 t^2 - (\frac{x_{well}}{\sin \phi_0})^2} \tag{68}$$

and

$$vt = \frac{x_{well}}{\sin \phi} \tag{69}$$

I use the same coordinate systems xz and $x'z'$ that I used in Appendix A. The tangent to the isochrone ellipse, described by the above equations, is horizontal at point B. This gives

$$\tan \phi_0 = \frac{z'_B}{x'_B}\frac{a^2}{b^2} \tag{70}$$

where x'_B and z'_B are the coordinates of point B in the $x'z'$ coordinate system. These coordinates must also satisfy equation (67):

$$(\frac{x'_B}{a})^2 + (\frac{z'_B}{b})^2 = 1 \tag{71}$$

Solving the last two equations for x'_B and z'_B and rotating back to the xz coordinate system, we end up with equations (12) and (13).

To prove equation (18), we need to observe that, according to equation (9)

$$\tan \phi_0 = \frac{\tan \phi}{2(\frac{x_A}{x_{well}}) - 1} = \frac{\tan \phi_{err}}{2(\frac{x_B}{x_{well}}) - 1} \tag{72}$$

where x_A and x_B are the horizontal coordinates of points A and B in the xz coordinate system. Using this last equation and equations (12) and (13), we end up with equation (18).

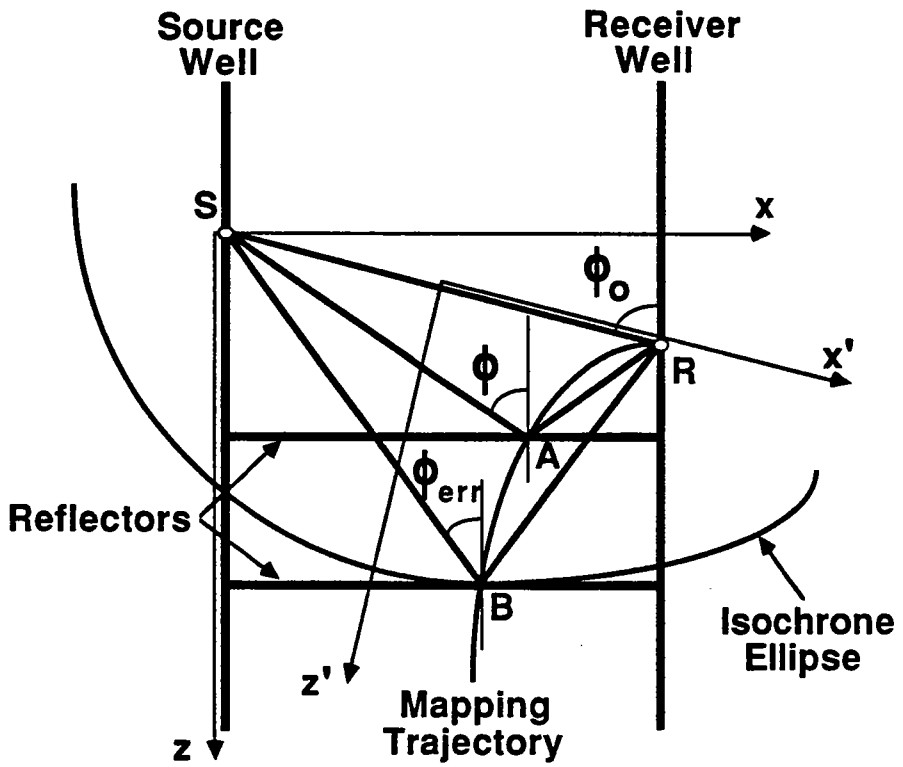

Figure B.1: Mispositioning of the reflection point due to a wrong mapping velocity. A wrong mapping velocity will cause the data point that would map on point A, to instead map on point B, along the same mapping trajectory, so that the total reflection traveltime remains constant.

APPENDIX C - RELATIONSHIP BETWEEN DIRECT-WAVE AND REFLECTION ANGLES

In this appendix I prove equation (29), which is the same as equation (9). From Figure 20, it is obvious that

$$\frac{x}{x_{well} - x} = \frac{z - z_S}{z - z_R} \tag{73}$$

which gives

$$\frac{2x - x_{well}}{x_{well} - x} = \frac{z_R - z_S}{z - z_R} \tag{74}$$

But

$$z_R - z_S = \frac{x_{well}}{\tan \phi_0} \tag{75}$$

and

$$z - z_R = \frac{x_{well} - x}{\tan \phi} \tag{76}$$

Combining the last three equations, we end up with equation (29).

APPENDIX D - FRESNEL ZONE CALCULATIONS

In this appendix I describe the calculation of the in-plane and out-of-plane size of the Fresnel zone for the crosswell geometry.

In-plane Fresnel zone

The basic geometry is shown in Figure D.1 The equation of the isochrone ellipse for time $t + T/2$ (T is the period) in the coordinate system $x'z'$ is

$$(\frac{x'}{a})^2 + (\frac{z'}{b})^2 = 1 \tag{77}$$

where

$$a = \frac{1}{2}v(t + \frac{T}{2}) \tag{78}$$

$$b = \frac{1}{2}\sqrt{v^2(t + \frac{T}{2})^2 - (\frac{x_{well}}{\sin\phi_0})^2} \tag{79}$$

and

$$vt = \frac{x_{well}}{\sin\phi} \tag{80}$$

The equation of the flat reflector at a depth z_F in the coordinate system $x'z'$ is

$$z' = \frac{z_F}{\sin\phi_0} - \frac{x_{well}}{2\sin\phi_0\tan\phi_0} - \frac{x'}{\tan\phi_0} \tag{81}$$

To find the size of the Fresnel zone, we need to find the intersections of the reflector, described by the last equation, with the ellipse, described by equations (77) to (80). Solving equations (77) and (81) for x' and z' and rotating back to the xz coordinate system, we end up with two values for the horizontal coordinate of the intersection point (since equation (77) is a second degree equation). These values correspond to the horizontal coordinates of points B and C on Figure D.1. The difference between these two horizontal coordinates is reduced, after some algebraic manipulation, to the result given by equations (38) to (45).

Out-of-plane Fresnel zone

I use the same $x'y'z'$ coordinate system that was used to calculate the effects of out-of-plane dipping reflectors. The equation of the isochrone ellipsoid in the $x'y'z'$ coordinate system is

$$(\frac{x'}{a})^2 + (\frac{y'}{b})^2 + (\frac{z'}{b})^2 = 1 \tag{82}$$

where a and b are again given by equations (78) and (79). The coordinates of the point of specular reflection in the xyz coordinate system are

$$\begin{bmatrix} x \\ z \end{bmatrix} = \begin{bmatrix} z_F\tan\phi \\ z_F \end{bmatrix} \tag{83}$$

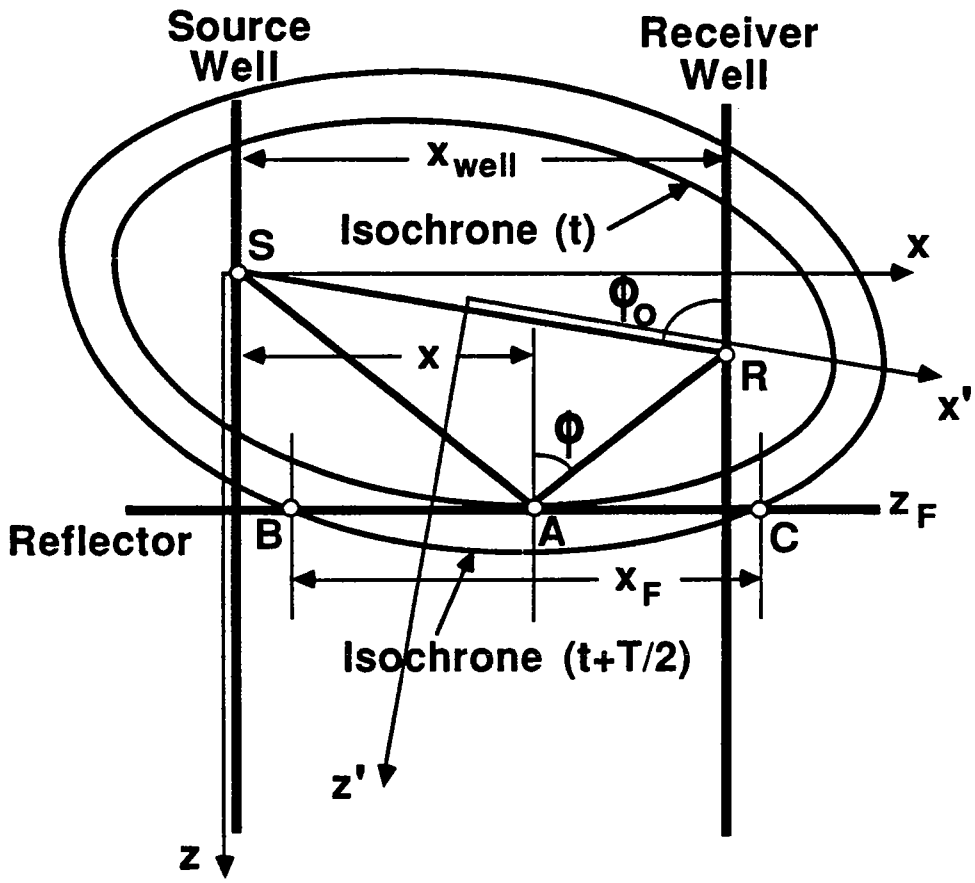

Figure D.1: Basic geometry for in-plane Fresnel zone calculation.

After rotation to the $x'y'z'$ coordinate system, these coordinates become

$$\begin{bmatrix} x' \\ z' \end{bmatrix} = \begin{bmatrix} z_F \sin\phi_0 \tan\phi + z_F \cos\phi_0 - \dfrac{x_{well}}{2\sin\phi_0} \\ -z_F \cos\phi_0 \tan\phi + z_F \sin\phi_0 \end{bmatrix} \tag{84}$$

Replacing these values of x' and z' into equation (82), we get a second-degree equation for y'. The difference between the two roots of this equation give the size y_F of the Fresnel zone in equation (46).